The Astrophysical Journal, 900:153 (19pp), 2020 September 10 https://doi.org/10.3847/1538-4357/abab93

Testing Comptonization as the Origin of the Continuum in Nonmagnetic Cataclysmic Variables: The Photon Index of X-Ray Emission

T. Maiolino[1,2,3], L. Titarchuk[3,4], F. D'Amico[5], Z. Q. Cheng[1,2], W. Wang[1,2], M. Orlandini[6], and Filippo Frontera[3,6,7]
[1] School of Physics and Technology, Wuhan University, Wuhan 430072, People's Republic of China; tais.maiolino@whu.edu.cn; angwei2017@whu.edu.cn
[2] WHU-NAOC Joint Center for Astronomy, Wuhan University, Wuhan 430072, People's Republic of China
[3] Dipartimento di Fisica, Università di Ferrara, via Saragat 1, I-44122 Ferrara, Italy; titarchuk@fe.infn.it; frontera@fe.infn.it
[4] Astro Space Center, Lebedev Physical Institute, Russian Academy of Sciences, Profsouznay ul. 84/32, Moscow 117997, Russia
[5] Instituto Nacional de Pesquisas Espaciais, Avenida dos Astronautas 178, 12227-010 S.J. dos Campos-SP, Brazil; flavio.damico@inpe.br
[6] INAF/OAS Bologna, via Gobetti 101, I-40129 Bologna, Italy; mauro.orlandini@inaf.it
[7] ICRANET Piazzale d. Repubblica 10-12, I-65122 Pescara (PE), Italy
Received 2020 May 26; revised 2020 July 16; accepted 2020 July 30; published 2020 September 11

Abstract

The X-ray spectra of nonmagnetic cataclysmic variables (nmCVs) in the ∼0.3–15 keV energy band have been described by either one or several optically thin thermal plasma components or by cooling flow models. We tested whether the spectral continuum in nmCVs could be successfully described by Comptonization of soft photons off hot electrons presented in a cloud surrounding the source (the transition layer (TL)). We used public XMM-Newton EPIC-pn, Chandra HETG/ACIS and LETG/HRC, and RXTE PCA and HEXTE observations of four dwarf novae (U Gem, SS Cyg, VW Hyi, and SS Aur) observed in the quiescent and outburst states. In total, we analyzed 18 observations, including a simultaneous 0.4–150 keV Chandra/RXTE spectrum of SS Cyg in quiescence. We fitted the spectral continuum with up to two thermal Comptonization components (the COMPTT or COMPTB models in XSPEC) using only one thermal plasma temperature and one optical depth. In this framework, the two seed photon components are presumably coming from the innermost and outer parts of the TL (or innermost part of the disk). We obtained that the thermal Comptonization can successfully describe the spectral continuum of these nmCVs in the ∼0.4–150 keV energy band. Moreover, we present the first principal radiative transfer model that explains the quasi-constancy of the spectral photon index observed around 1.8, which strongly supports the Comptonization framework in nmCVs.

Unified Astronomy Thesaurus concepts: X-ray binary stars (1811)

1. Introduction

The power source of X-rays in cataclysmic variables (CVs) is known to be due to the accretion of matter onto a compact object: a white dwarf (WD). In nonmagnetic CVs (nmCVs), as well as in all CVs containing accretion disks, the accretion disk is generally too cold ($kT \ll 1$ keV) to emit X-rays (Lewin & van der Klis 2006). The major source of X-rays has been identified with the transition layer (TL), the region between the spiraling accretion disk and the surface of a more slowly rotating WD, wherein half of the gravitational energy is expected to be released. Physical characteristics of the TL and the system have been described to account for both the observed soft and hard X-ray spectral emission (Pringle & Savonije 1979; Patterson & Raymond 1985a, 1985b; Titarchuk et al. 2014).

In the standard TL framework, the accretion rate determines the TL optical depth, which, along with the electron temperature T_e of the TL, drives the X-ray spectral emission. Patterson & Raymond (1985a, and references therein) suggested that at a high accretion rate ($\dot{M} \gtrsim 10^{16}$ g s^{-1}), the TL is expected to be optically thick and radiate a blackbody component at $T \sim 10^5$ K. On the contrary, at a low accretion rate ($\dot{M} < 10^{16}$ g s^{-1})—i.e., in the quiescent state—the TL is expected to have a lower density and be optically thin. Because optically thin plasma does not cool efficiently, higher temperatures are expected in this state. The cooling of the TL in this case has been described by a thermal bremsstrahlung component, emitting hard X-rays at temperature $T \sim 10^8$ K (Patterson & Raymond 1985b). Part (up to half) of the hard X-rays emitted by the TL must be absorbed by a WD surface and reradiated in soft X-rays with an effective temperature $T_{\rm eff} \lesssim 10^{5-6}$ K (see, e.g., Patterson & Raymond 1985b; Williams et al. 1987; Mukai 2017).

Early spectral analysis of nmCVs showed that their spectral continua were generally well described by only one thermal bremsstrahlung component, i.e., by a single plasma temperature in the 1–5 keV energy range, and of a few keV up to ∼10 keV in the case of dwarf novae (DNe; Lewin & van der Klis 2006, and references therein).

In recent decades, the single-temperature MEKAL (or its variation, VMEKAL) model (see XSPEC; Mewe et al. 1986; Liedahl et al. 1995) has been broadly used to fit the CV spectra. In this model, the X-ray radiation is produced by a hot, optically thin thermal plasma; the basis of the continuum radiation is free–free (bremsstrahlung), free–bound, and two-photon emission. The emission lines observed are included in this model and modeled by excitation from electron impact, radiative and dielectronic recombination, and inner-shell excitation and ionization. As the model is in the optically thin limit, photoionization or photoexcitation effects are not taken into account. Similar to the MEKAL model, the APEC code[8] (or its variations, VAPEC and VVAPEC) is another thermal optically

[8] Calculated using the ATOMDB code; more information can be found at http://atomdb.org.

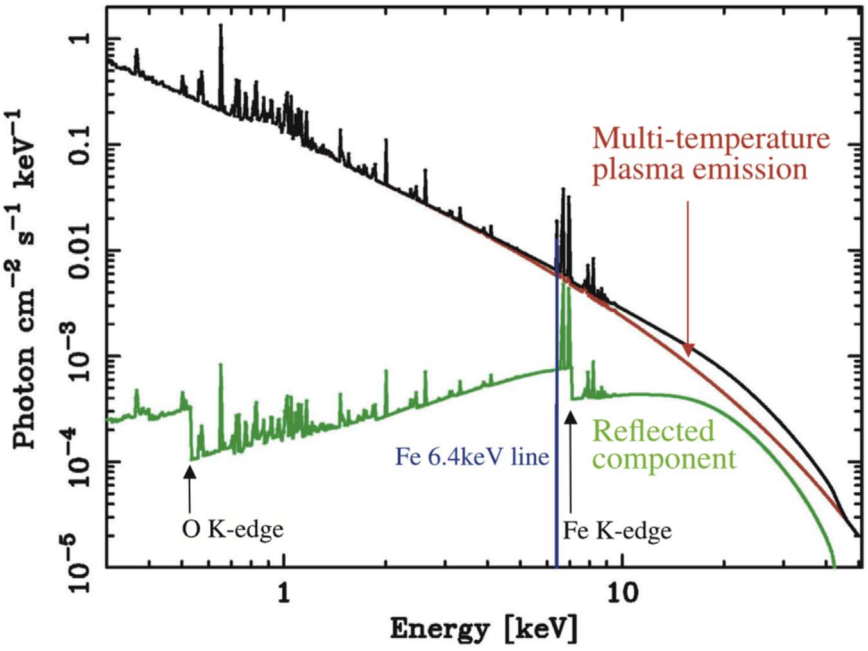

Figure 1. Spectral components of SS Cyg in the 0.2–40 keV band, which basically represents the spectral modeling of CVs: a multitemperature optically thin thermal plasma represents the hard X-ray emission (red), and the reflection of the hard X-rays by the accretion disk and/or the surface of the WD produces the observed fluorescent iron K_α lines and a hump in the continuum (green; Done & Osborne 1997; Ishida et al. 2009).

thin plasma model that has been commonly used to describe the spectra of nmCVs.

Spectral analysis using data from X-ray observatories with better signal-to-noise ratios and energy resolution (e.g., XMM-Newton and Suzaku) showed that only one optically thin plasma temperature does not satisfactory fit the spectra of all sources (Lewin & van der Klis 2006); there are analyses in which two or even more plasma temperatures are needed to obtain good spectral fits (see, e.g., Pandel et al. 2003). For that reason, it has been suggested that the cooling flow spectral model should represent a more physically correct description of the observed X-ray spectra.

The gas flow in cooling flow models is assumed to be composed of a range of temperatures that vary from the hot shock temperature $kT_{\rm max}$ (the maximum temperature to which the plasma is heated; $kT_{\rm max} \sim$ 10–80 keV) to the temperature when the optically thin cooling material settles onto the WD surface (see Mukai et al. 2003; Byckling et al. 2010, and references therein). Cooling flow models are available in XSPEC as CEMEKL or CEVMKL and MKCFLOW or VMCFLOW; these models were originally developed to describe the cooling flows in clusters of galaxies. It is now known that such models do not successfully describe these sources (as stated in Mukai et al. 2003; see references therein). All of them basically use an optically thin thermal plasma model for the individual temperature components.

Baskill et al. (2005) used the CEMEKL cooling flow model to successfully fit ∼30 DNe spectra observed with ASCA (their source sample includes three out of four of the nmCVs analyzed in this paper: SS Cyg, U Gem, and VW Hyi). Byckling et al. (2010), through XMM-Newton, Suzaku, and ASCA data, fitted the spectra of 12 DNe (their source sample includes SS Cyg, U Gem, and SS Aur) using either a one-temperature optically thin plasma model or a cooling flow model. All fits include spectral components, taking into account absorption created by the presence of material along the line of sight. A photoelectric absorption column is usually used (e.g., the WABS model in XSPEC was extensively used in recent years), with additional partial covering absorption (e.g., PCFABS in XSPEC) in some cases, to take into account the presence of an intrinsic absorber located somewhere within the binary system (see, e.g., Byckling et al. 2010).

Mukai et al. (2003), using Chandra high-energy transmission grating (HETG) data, stated that there are two types of CV X-ray spectra and suggested that the spectral differences might lie on the specific accretion rate (accretion rate per unit of area) of the systems. They showed that all three nmCVs analyzed (and an unusual intermediate polar (IP), EX Hya) had their spectra better described by cooling flow models, whereas other sources analyzed (which were all of the IP type) had their spectra better described by the photoionization model (the PHOTOION model in XSPEC).

Figure 1 shows the spectral components of the nmCV SS Cyg in the 0.2–40 keV energy band (Ishida et al. 2009). This picture was proposed by Done & Osborne (1997) on the basis of their analysis of SS Cyg using Ginga and ASCA data and represents a general framework of the radiative process in CVs widely accepted (by the time of this paper) by the scientific community. The red line in Figure 1 represents the hard X-ray spectrum, primarily composed of an optically thin thermal plasma emission with a temperature distribution. In this framework, a part of the hard X-rays produced in the optically thin thermal plasma suffers reflection from the accretion disk and/or WD surface, which represent a significant fraction of the observed X-ray flux. This reflected component (represented by the green line in Figure 1) explains, in the same way as in low-mass X-ray binaries (LMXBs) and type I Seyfert galaxies (George & Fabian 1991), the production of the neutral fluorescent iron K_α line observed at 6.4 keV in several CVs. The presence of this feature is explained by the reflection of X-rays from the accretion disk and/or the WD surface, where relatively cold iron with temperatures $\leqslant 10^6$ K is present. In general, up to three distinct iron emission lines in the

~6.4–7.0 keV energy range may be present in the spectra of CVs related to neutral, He-like, and H-like K_α Fe lines. The He- and H-like lines (at ~6.7 and 7.0 keV, respectively) are produced by a plasma with relatively higher temperatures of 10^{7-8} K (see, e.g., Rana et al. 2006).

For a more detailed review of nmCVs and their X-ray emission, as well as other types of CVs, see, for example, Warner (1995) and Mukai (2017).

The Comptonization model is not one of the standard models that is currently used to describe the CV continuum. However, CVs, mainly the nonmagnetic and IP types, share structural similarities with LMXBs; i.e., these systems contain an accretion disk (which appears either entirely in nmCVs or partially in IPs), a TL (corona), and a compact object. Taking into account these geometric/structural similarities and the radiative processes used to describe the continuum of LMXBs—which has changed from bremsstrahlung to Comptonization—we tested whether the spectral continuum of nmCVs and IPs could be successfully described by the Comptonization (upscattering) of soft photons off the hot electrons of a Compton cloud around the compact object, as it is in LMXBs. In this paper, we present the results of this verification performed on nmCVs. We used four XMM-Newton EPIC-pn, eight Chandra (LETG/HRC and HETG/ACIS), and six RXTE (Proportional Counter Array (PCA) and HEXTE) public observations of four DNe: U Gem, SS Cyg, VW Hyi, and SS Aur. These sources were observed only in quiescence by XMM-Newton and in the quiescent and outburst states by Chandra and RXTE. In our observational sample, we have a simultaneous Chandra/RXTE observation of SS Cyg, which provides us the 0.4–150 keV broadband spectral description of this source in the quiescent state.

In a previous paper by Titarchuk et al. (2014), the authors found the photon index, Γ, in the neutron star (NS) sources strongly concentrated at 2. Moreover, using the radiative transfer model, they analytically demonstrated that this is a result of the gravitational release of accreted material in the TL near an NS surface. Our goal is to show that a similar effect should be seen in WDs in which we should take into account the absorption of the X-ray radiation by the WD surface (while in an NS, its surface reflects X-ray radiation).

This paper is organized as follows. In Section 2 we describe our source sample; in Section 3 we present the data reduction of the XMM-Newton (EPIC-pn), Chandra (LETG/HRC and HETG/ACIS), and RXTE (PCA and HEXTE) observations; in Section 4 we describe the spectral analysis; in Section 5, we present our radiative transfer model, which explains the invariance of the photon index; in Section 6 we discuss the results of the paper; and in Section 7 we present our final conclusions.

2. Source Sample

Since the goal of this work is to study the spectral continuum of nmCVs, any sources belonging to this type have been included in our sample. Because we started this study using XMM-Newton EPIC-pn data, we have chosen sources present in the archive with public EPIC-pn observations. Thus, we included four nmCVs in our sample, U Gem, SS Cyg, VW Hyi, and SS Aur, which are among the brightest X-ray nmCVs.

For completeness, in this section, we give a brief description of these sources. We present the binary system parameters (orbital period ($P_{\rm orb}$), rotational period ($P_{\rm spin}$), and inclination angle (i)), distance, and temporal properties and examples of the spectral modeling published in the literature for each source.

2.1. U Gem

The nmCV U Gem has a WD with a mass ($M_{\rm WD}$) of $1.07 \pm 0.08\,M_\odot$ (Ritter & Kolb 2003). It appears to be at most slowly rotating ($v \sin i \lesssim 100\,{\rm km\,s^{-1}}$), which corresponds to 20% of the breakup velocity (Lewin & van der Klis 2006). The secondary star has a mass M_2 of $0.39 \pm 0.02\,M_\odot$ (Ritter & Kolb 2003) and spectral type M4 V (Harrison et al. 2000). The system is located at 100 ± 4 pc of distance; it has an orbital period of 4.246 hr (Harrison et al. 2004) and an inclination i of $69^\circ \pm 2^\circ$ (Ritter & Kolb 2003). Dips in the X-ray light curves have been observed during quiescence (Szkody et al. 1996, 2002), as well as during normal (Long et al. 1996) and anomalous outbursts (of ~45 days; Mason et al. 1988). The X-ray dips in U Gem are less deep in quiescence than in outburst. The morphology of the dips changes from cycle to cycle, related to changes in the absorbing material. In U Gem, both soft and hard X-ray fluxes are higher during outburst than in quiescence by a factor of ~10–100 (see Lewin & van der Klis 2006, and references therein).

Güver et al. (2006) studied the spectral emission of U Gem in both the quiescent and outburst states using the same XMM-Newton, Chandra HETG/ACIS, and RXTE PCA observations present in our sample. They fitted the quiescence spectra with both the CEMEKL (or CVMKL) and MKCFLOW cooling flow models, finding a maximum temperature $kT_{\rm max}$ in the ~15–38 keV range. They reported, for the first time, the properties of the hard X-ray emission of this source in outburst. In this state, an extra X-ray nonthermal component is needed, in addition to a simple MEKAL-based multitemperature component, to obtain an acceptable spectral fit. Though deviations from the continuum are still noticeable, this extra component was better described by a power law rather than other models (such as thermal bremsstrahlung; see Table 4 and Figures 3 and 4 therein). The authors reported $kT_{\rm max} = 9.49 \pm 4.1$ and 18.44 ± 10.5 keV for the CEMEKL component in the Chandra HETG/ACIS HEG and MEG spectra, respectively, and a power-law component with a photon index Γ of 0.54 ± 0.16 and 0.64 ± 0.06, respectively. Analyzing the 3–20 keV PCA spectra throughout the 2004 outburst, the authors demonstrated evidence of a transient hard X-ray component, since in nine out of 23 spectra, the power-law component was not required. They suggested that this component is driven by a mechanism temporarily present during outburst, which could be a reflection of X-rays coming from either the optically thick plasma or an optically thick boundary layer, as well from a transient magnetosphere present during outburst (see Güver et al. 2006, and references therein). On the other hand, they noticed that spectral features expected by the reflection scenario, such as the K_α fluorescent lines, are either very weak or not observed during the outburst state in U Gem. It is important to stress, however, that the reflection scenario is not the only one capable of explaining the K_α fluorescent line production (see, e.g., Maiolino et al. 2019).

Mukai et al. (2003) showed that the Chandra spectrum of the DN U Gem (as well as SS Cyg and V603 Aql) can be described by the multitemperature bremsstrahlung cooling flow model MKCFLOW with $kT_{\rm max} = 20$ keV. Byckling et al. (2010) fitted the XMM-Newton U Gem spectrum in quiescence, also using the MKCFLOW model, and found a maximum temperature $kT_{\rm max} = 25.82^{+1.98}_{-1.43}$ keV and an equivalent width of the Fe 6.4 keV line (EW6.4) of 60^{+33}_{-32} eV. On the other hand, using a single-temperature optically thin plasma model (MEKAL), they found $kT = 0.78^{+0.03}_{-0.01}$ keV and an EW6.4 of 50^{+25}_{-24} eV. Xu et al. (2016)

analyzed the spectra of 41 CVs observed with Suzaku. They used the single-temperature model APEC to fit the 2–10 keV continuum and three Gaussian components (at 6.4, 6.7, and 7.0 keV) to fit the Fe emission lines of U Gem in quiescence. They found a plasma temperature $kT = 16.5^{+4.49}_{-3.31}$ keV and EW6.4 $= 43^{+16}_{-11}$ eV, EW6.7 $= 258^{+22}_{-21}$ eV, and EW7.0 $= 178^{+11}_{-11}$ eV.

2.2. SS Cyg

The system SS Cyg belongs to the U Gem type of DN. It has a WD with a mass $M_{\rm WD}$ of $1.19 \pm 0.02\,M_{\odot}$, a secondary star with a mass M_2 of $0.704 \pm 0.002\,M_{\odot}$ (Friend et al. 1990), and a K5/5 spectral type (Ritter & Kolb 2003). The binary system is located at 166 ± 12 pc (Harrison et al. 1999, 2004) and has an inclination angle i of $37^{\circ} \pm 5^{\circ}$ (Ritter & Kolb 2003) and a period of 6.603 hr (Harrison et al. 2004). This source is one of the DNe broadly studied in outbursts, as it shows an optical outburst every ∼50 days, in which m_V changes from 12th to 8th magnitude (Mauche & Robinson 2001; Lewin & van der Klis 2006; see, for example, Figure 10.1 therein). They claimed that the system shows a reflection component in the quiescent and outburst states, with a larger contribution in the outburst (Done & Osborne 1997; Lewin & van der Klis 2006, and references therein). Mukai et al. (2003) found a maximum plasma temperature $kT_{\rm max}$ of 80 keV using fits of the Chandra spectrum of this source in quiescence and the multitemperature MKCFLOW model.

Okada et al. (2008) analyzed the two Chandra/HETG observations present in our sample. They constrained the power-law index and temperature of the boundary layer in the framework of the CEMEKL model.

Ishida et al. (2009) presented a Suzaku XIS and HXD-PIN analysis of this source observed in 2005 November in the quiescent and outburst states. Using the multitemperature thin plasma model CVMEKAL (model in XSPEC), they found a maximum temperature of the plasma $kT_{\rm max}$ of $20.4^{+4.0}_{-2.6}$ (stat) $\pm$ 3.0 (sys) keV in quiescence and $6.0^{+1.3}_{-0.2}$ keV in outburst.

Byckling et al. (2010) fitted a Suzaku XIS spectrum of SS Cyg in quiescence using the optically thin plasma model MEKAL and the cooling model MKCFLOW (including photoelectric absorption and partial covering as well). As a result, they obtained a plasma temperature of $10.44^{+0.16}_{-0.17}$ keV and a maximum temperature of the plasma $kT_{\rm max}$ of $41.99^{+1.20}_{-0.76}$ keV, respectively. In their fits, EW6.4 is equal to 75^{+9}_{-4} and 73^{+6}_{-7} eV, respectively. Xu et al. (2016), using Suzaku data (during an outburst) and the single-temperature model APEC, fit the 2–10 keV continuum including three Gaussian components of the iron emission lines (at 6.4, 6.7, and 7.0 keV). As a result, they estimated a plasma temperature $kT = 8.15^{+1.23}_{-0.91}$ keV and EW6.4 $= 67^{+11}_{-10}$ eV, EW6.7 $= 415^{+41}_{-30}$ eV, and EW7.0 $= 48^{+15}_{-11}$ eV.

2.3. VW Hyi

The source VW Hyi is a well-studied one. It is located at 54 ± 0.1 pc (see Nakaniwa et al. 2019, and references therein) and belongs to the SU UMa subgroup of DNe (Warner 1987), which undergoes both normal DN outbursts and superoutbursts (Godon & Sion 2005). The $M_{\rm WD}$ was estimated as $0.63 \pm 0.15\,M_{\odot}$ (Schoembs & Vogt 1981).[9] The secondary star has a mass M_2 of $0.11 \pm 0.02\,M_{\odot}$ (Schoembs & Vogt 1981), and it is an M6V star (Godon & Sion 2005). The binary system has an inclination angle i of $60^{\circ} \pm 10^{\circ}$ (Schoembs & Vogt 1981) and an orbital period of 0.074271 days (∼1.783 hr, which lies below the CV period gap; Ritter & Kolb 2003). It shows superhumps (which are variations in the light curves at a period of a few percent longer than the orbital period) with a period of 0.07714 days (∼1.85 hr) and lies along a line of sight with a very low interstellar absorption, $N_H \approx 6 \times 10^{17}$ atoms cm^{-2} (Polidan et al. 1990). This low interstellar absorption allows us to observe this system in almost all wavelength ranges.

The source shows a very low mass accretion rate during quiescence, $\dot{M} \approx 10^{-11}\,M_{\odot}$ yr^{-1}, emitting significantly in the UV (between 35% and 47%; see Godon & Sion 2005, and references therein). The first X-ray observations of VW Hyi in quiescence were done in 1984 with EXOSAT (van der Woerd & Heise 1987), in which persistent hard (1–6 keV) and soft (0.04–1.5 keV) X-ray fluxes were observed. In the spectral analysis, an equally best fit was pointed out using either a power-law or thermal bremsstrahlung model ($kT > 5$ keV) without interstellar absorption ($N_H < 10^{21}$ atoms cm^{-2}).

Belloni et al. (1991) fitted the spectrum of VW Hyi observed in quiescence by ROSAT using the Raymond–Smith optically thin thermal plasma model with a single temperature (Raymond & Smith 1977). They found a temperature of 2.17 ± 0.15 keV for zero interstellar absorption (when absorption was included and a significantly different temperature and flux were not found). Hasenkopf & Eracleous (2002) analyzed the spectrum of VW Hyi observed with ASCA and, using two- and multiple-temperature thermal plasma models, revealed that the resulting temperatures lie mostly between 4 and 10 keV.

Pandel et al. (2003, 2005) analyzed an XMM-Newton/EPIC spectrum of VW Hyi in quiescence (the same observation analyzed in this paper). They modeled the spectrum with cooling flow models—i.e., with multitemperature thin thermal plasma models (CEMEKL, CEVMKL, and MKCFLOW)—and obtained a maximum temperature $kT_{\rm max}$ between 6–8 keV. Pandel et al. (2003) attempted to fit the EPIC spectra with one or two single-temperature MEKAL models (as commonly used to fit DNe spectra) but obtained a satisfactory fit only when three components of their model were used.

Nakaniwa et al. (2019) also analyzed the same XMM-Newton/EPIC observation present in our sample, along with three more Suzaku/XIS observations in quiescence. They reported that all 0.2–10 keV spectra are moderately well fitted by the CEVMKL and VMCFLOW cooling flow models, with a maximum temperature of 5–9 keV. Namely, for the XMM-Newton observation, they obtained a plasma temperature $kT_{\rm max}$ of $5.32^{+0.23}_{-0.22}$ and $6.95^{+0.20}_{-0.19}$ keV with the CEVMKL and VMCFLOW models, respectively.

Xu et al. (2016) used Suzaku data and the single-temperature model APEC to analyze the 2–10 keV continuum and three Gaussian components (at 6.4, 6.7, and 7.0 keV) to fit the Fe emission lines found in VW Hyi (in the quiescent state). They found a plasma temperature kT of $5.79^{+4.71}_{-2.14}$ keV, and for the emission Fe lines, they estimated EW6.4 $= 0.01$ eV (upper limit), EW6.7 $= 1392^{+152}_{-172}$ eV, and EW7.0 $= 42^{+58}_{-42}$ eV.

2.4. SS Aur

The binary system SS Aur belongs to the U Gem type of DN with high mass accretion rates $\dot{M}$. It is located at 167^{+10}_{-09} pc (Harrison et al. 2004) and has an inclination angle i of $38^{\circ} \pm 16^{\circ}$. The system has an orbital period of 0.1828(1) days (which is

[9] A gravitational redshift determination done by Sion et al. (1997) yielded $M_{\rm WD} = 0.86^{+0.18}_{-0.32}\,M_{\odot}$.

Table 1
Log of the XMM-Newton, Chandra, and RXTE Observations

Source	Observatory	Instrument	ObsID	Start Time Date (UTC)	End Time Date (UTC)	Exp. (ks)	State
VW Hyi	XMM-Newton	EPIC/PN	0111970301	2001 Oct 19 06:10:05	2001 Oct 19 10:38:34	14.5	Quiescence
	Chandra[a]	LETG/HRC	21671	2018 Aug 8 00:16:30	2018 Aug 8 03:19:03	9.67	Outburst
SS Cyg	XMM-Newton	EPIC/PN	0111310201	2001 Jun 5 08:14:19	2001 Jun 5 11:34:10	11.8	Quiescence
	Chandra	LETG/HRC	1897	2001 Jan 16 21:13:00	2001 Jan 17 10:49:56	47.1	Outburst
	Chandra	HETG/ACIS	646	2000 Aug 24 10:28:23	2000 Aug 25 00:19:30	47.3	Quiescence
	Chandra	HETG/ACIS	648	2000 Sep 14 21:09:02	2000 Sep 15 14:15:05	59.5	Outburst
	Chandra	HETG/ACIS	2307	2000 Sep 12 17:00:58	2000 Sep 13 03:47:18	36.6	Outburst
	RXTE	PCA	50012-01-01-00	2000 Aug 24 13:04:16	2000 Aug 24 18:31:44	13.4	Quiescence
	RXTE	HEXTE	50012-01-01-00	2000 Aug 24 13:04:16	2000 Aug 24 18:31:44	1.19	Quiescence
	RXTE	PCA	10040-01-01-000	1996 Oct 9 16:47:28	1996 Oct 9 23:00:00	6.10	Outburst
	RXTE	PCA	10040-01-01-001	1996 Oct 9 23:28:32	1996 Oct 10 07:25:36	11.4	Outburst
	RXTE	PCA	10040-01-01-00	1996 Oct 10 07:25:20	1996 Oct 10 11:17:04	8.67	Outburst
U Gem	XMM-Newton	EPIC/PN	0110070401	2002 Apr 13 05:35:37	2002 Apr 13 11:35:35	15.1	Quiescence
	Chandra	LETG/HRC	3773	2002 Dec 25 19:50:15	2002 Dec 26 09:28:39	47.0	Outburst
	Chandra	HETG/ACIS	647	2000 Nov 29 12:01:20	2000 Nov 30 15:13:31	94.9	Quiescence
	Chandra	HETG/ACIS	3767	2002 Dec 26 09:28:39	2002 Dec 27 03:33:37	61.4	Outburst
	RXTE	PCA/HEXTE	80011-01-02-00	2004 Mar 5 2:14:56	2004 Mar 5 09:03:44	14.5	Outburst
SS Aur	XMM-Newton	EPIC/PN	0502640201	2008 Apr 7 08:40:28	2008 Apr 7 20:31:58	31.5	Quiescence
	RXTE	PCA/HEXTE	30026-03-01-00	1998 Jan 24 05:03:12	1998 Jan 24 12:12:00	14.2	Quiescence

Note.
[a] Observation not considered in our final analysis.

equivalent to 4.387 hr; Shafter & Harkness 1986; Harrison et al. 2004; Byckling et al. 2010). The system hosts a WD with a mass $M_{\rm WD}$ of $1.08 \pm 0.40\,M_{\odot}$ and a secondary star of ~M1 V type (Harrison et al. 2000) with a mass M_2 of $0.39 \pm 0.02\,M_{\odot}$ (Ritter & Kolb 2003, and references therein). Byckling et al. (2010) fitted a Suzaku XIS spectrum of SS Aur in quiescence using both the optically thin plasma model MEKAL and the cooling model MKCFLOW (including photoelectric absorption and partial covering as well). They obtained a plasma temperature of 6.35 ± 0.40 keV and a maximum temperature of the plasma $kT_{\rm max}$ of $23.47^{+4.01}_{-3.02}$ keV, respectively. In these fittings, EW6.4 is equal to 73^{+37}_{-36} and 86^{+52}_{-53} eV, respectively. Xu et al. (2016), using Suzaku data and the single-temperature model APEC in the 2–10 keV continuum and three Gaussian (the Fe emission lines) components (at 6.4, 6.7, and 7.0 keV), found that SS Aur in the quiescent state has the best-fit parameters of a plasma temperature of $8.48^{+5.34}_{-2.61}$ keV and EW6.4 $= 47^{+60}_{-29}$ eV, EW6.7 $= 325^{+90}_{-65}$ eV, and EW7.0 $= 169^{+57}_{-49}$ eV.

3. Data Reduction

3.1. XMM-Newton

We analyzed a total of four XMM-Newton EPIC-pn public observations, one observation of each source. See Table 1 for a log of the observations. All XMM-Newton observations were taken with the sources in the quiescent state.

The sources VW Hyi, U Gem, and SS Aur were observed with the pn camera operating in imaging mode, while SS Cyg was observed with the pn camera in timing mode. All light curves and spectra were extracted through Science Analysis Software (SAS) version 14.0.0. We strictly followed the recommendations for the pn camera in each mode of observation (timing and imaging, respectively). Following Guainazzi (2016), we considered the 0.3–15.0 keV spectral energy range for observations taken in imaging mode and the 0.7–10.0 keV range for the observation taken in timing mode.

We checked spectral variability by extracting two light curves for each source. The two light-curve energy ranges were selected according to the observational mode: from 0.3 to 4.0 and 4.0 to 15 keV for observations taken in imaging mode and from 0.7 to 4.0 and 4.0 to 10.0 keV for observations taken in timing mode. We computed the ratios between the light curves in the two energy bands (the hardness ratio (HR)). The HR of SS Aur showed a time interval of increased noise at the end of the exposure, which was discarded in the spectral extraction. For all other observations, a count rate variability was not associated with a significant change in the HR or a noise increase. Therefore, we used the total EPIC-pn exposure time in the spectral extraction of these observations.

Standard filters were applied during data screening through the `evselect` task. We considered only single and double events (using pattern $\leqslant$4). We used `FLAG==0` to discard regions of the detector (like border pixels and columns with higher offset) for which the pattern type and total energy is known with significantly lower precision.

The observation of SS Cyg was taken in timing mode and prior to 2012 May 23, the period in which almost all EPIC-pn exposures are unexpectedly affected by X-ray loading (XRL), which occurs when source counts contaminate the offset map taken prior the exposure. Because of this, we applied the XRL correction to this observation.

In all spectral extraction, the background region was selected from a region away from the source. The distribution matrix (rmf) and ancillary (arf) files were created through the `rmfgen` and `arfgen` tasks. The final spectra were rebinned in order to have at least 25 counts for each background-subtracted channel.

3.2. Chandra

We used all eight grating Chandra public observations of our nmCV sample presented to the preparation time of this paper; see Table 1 for a log of the observations. There was only one observation of VW Hyi during an outburst, while SS Cyg and

U Gem were observed four and three times, respectively, in both outburst and quiescent states. There are no public observations available in the archive for SS Aur. There was one observation of SS Cyg, U Gem, and VW Hyi in LETG/HRC-S mode, while SS Cyg and U Gem were observed three and two times in HETG/ACIS-S mode, respectively. Following the standard procedure,[10] we used CIAO v4.11 and the corresponding calibration files to reprocess the data. The spectra of each observation were generated with the Chandra_repro script. We combined the first-order spectra and adopted a minimum signal-to-noise ratio value of 10 to group the spectra. For each observation, we also extracted two light curves in the 0.4–4 and 4–10 keV bands and checked for variability. Significant changes in the HR were not observed; therefore, we used the total exposure time in the spectral extraction. The reprocessed spectrum of VW Hyi did not show a spectral component at energies greater than 0.5 keV. Therefore, we did not consider this spectrum in our final spectral analysis.

3.3. RXTE

We have analyzed six RXTE observations of three nmCVs: one of U Gem, one of SS Aur, and four of SS Cyg. The observations of SS Aur and SS Cyg, ObsID 50012-01-01, were in quiescence. All other observations were taken with the source in the outburst state. See Table 1 for a log of the observations.

All PCA data were analyzed following the standard procedure. Only low-resolution (16 s) light curves were produced together with spectra in the 2–60 keV band. For each observation, the spectra and light curves were derived using standard RXTE/FTOOLS. Briefly, the data reduction consists of the source+background production, with subsequent subtraction of the PCA background estimated through the PCABACKEST tool. The PCA response matrix was built with PCARSP, and systematic errors (of 0.04%) were added to each individual spectrum.

For each cluster, HEXTE 20–200 keV spectrum extraction (Rothschild et al. 1998) is done using a comparison of the spectra from two separate background fields that are sampled alternately during observations. This capability allowed us, for example, to discard data from cluster B for SS Cyg, since one of the background regions for this cluster (and for that sky position) is contaminated by the nearby source IGR J21485 +4306. The HEXTE background lines (Rothschild et al. 1998) were also treated and removed from the final spectrum. Spectra and response matrices were produced following the well-known procedures (see, e.g., D'Amico et al. 2001).

4. Spectral Analysis

In order to validate the Comptonization framework in nmCVs and obtain better estimates of the physical parameters and spectral (photon) indices in these systems, we analyzed the spectra of our sources obtained by three different observatories: XMM-Newton, Chandra, and RXTE. All analyses were performed using XSPEC astrophysical package version 12.8.2.

The spectral continuum was first modeled by a single thermal Comptonization component, the COMPTT model in XSPEC (Titarchuk 1994; Hua & Titarchuk 1995; Titarchuk & Lyubarskij 1995), considering a plasma cloud of a plane geometry. The physical free parameters of this model are the temperature of the seed photons kT_s, the electron temperature kT_e, and the optical depth τ of the Compton cloud. Only when required by the fit was a second Comptonization component added to the total model. Due to the broader spectral energy range of RXTE, this second component was required in only three out of four RXTE spectra of SS Cyg.

In all XMM-Newton, Chandra, and RXTE spectra, the residual excess—i.e., the emission lines—expected and observed in the Fe XXI–XXVI K-shell (~6.4–7.0 keV) energy range was modeled by up to three Gaussian components. Due to the low energy resolution of RXTE/PCA, only one broad Gaussian component is required to account for the excess caused by these features.

4.1. XMM-Newton Spectral Analysis

In all spectra, an addition of a photoelectric absorption (N_H) and/or blackbody component (e.g., the BBODY or BBODYRAD model) did not improve the fit performed in the ~0.3–15/0.4–10 keV energy range of XMM-Newton.

The spectrum of U Gem showed three iron emission lines with centroid energies of $6.394^{+0.013}_{-0.013}$ (at 2.5σ of the He-like K_α line), $6.68^{+0.04}_{-0.04}$ (compatible with the He-like Fe K_α line), and $6.972^{+0.023}_{-0.019}$ (at 1.2σ from the H-like Fe K_α line at 7.0 keV) keV and equivalent widths (EWs) of 53^{+41}_{-25}, 281^{+100}_{-49}, and 167^{+53}_{-40} eV, respectively.

The spectra of SS Cyg and SS Aur showed two iron emission lines. In SS Cyg, the lines appear with centroid energies of $6.634^{+0.026}_{-0.023}$ (compatible with the neutral Fe K_α line) and $6.966^{+0.030}_{-0.026}$ (at 1.1σ from the H-like Fe K_α line at 7.0 keV) keV and EWs of 186^{+321}_{-27} and 75^{+97}_{-20} eV, respectively.

In SS Aur, the lines appear with centroid energies of $6.67^{+0.04}_{-0.03}$ (compatible with the He-like Fe K_α line) and $7.00^{+0.05}_{-0.05}$ (compatible with the H-like Fe K_α line) keV and EWs of 528^{+388}_{-156} and 169^{+99}_{-89} eV, respectively.

The VW Hyi spectrum is the only one that showed one emission iron line. This line appears with a Gaussian centroid energy of $6.672^{+0.017}_{-0.015}$ keV (at 1.6σ from the He-like Fe K_α line), and it is very strong, with an EW equal to 995^{+152}_{-143} eV, which is 2–20 times stronger than those observed in other sources.

Table 2 shows the best-fit parameters and fit quality found for each XMM-Newton observation, and Figure 2 shows the best spectral fits. The presence of the Fe Gaussian lines is evident in all fits. Without adding any model to account for the iron line emission, the best fit gives a reduced $\chi^2_{\rm red} = \chi^2/{\rm degree\ of\ freedom\ (dof)}$ of 1.54 (801/521) for VW Hyi, 1.38 (1151/836) for SS Cyg, 1.97 (530/269) for U Gem, and 1.11 (672/604) for SS Aur. When Gaussian components are added to the fit, it leads to a $\chi^2_{\rm red}$ of 1.30 (672/519) for VW Hyi, 1.01 (840/831) for SS Cyg, 1.15 (366/317) for U Gem, and 0.93 (556/598) for SS Aur.

In addition to the emission iron lines in the ~6.4–7.0 keV energy range, we observed in all spectra another strong and broad residual excess peaked at ~1.01 keV with a Gaussian centroid in the ~0.96–1.02 keV energy range (see the $\rm Gaussian_0$ component in Table 2). These centroid energies are compatible with resonance lines emitted by Ne X, Fe XVII, or Fe XXI ions. Table 3 summarizes these possible emission lines.

[10] https://cxc.harvard.edu/ciao/threads/gspec.html

Table 2
Spectral Analysis of the XMM-Newton Observations of Our nmCV Sample

Source Component	Parameter	Unit	VW Hyi	SS Cyg	U Gem	SS Aur
CompTT	kT_s	keV	$0.15^{+0.01}_{-0.01}$	$0.100^{+0.021}_{-0.044}$	$0.141^{+0.004}_{-0.004}$	$0.168^{+0.006}_{-0.007}$
	kT_e	keV	$8.58^{+0.14}_{-0.14}$	$7.64^{+0.05}_{-0.05}$	$6.43^{+0.06}_{-0.06}$	$6.12^{+0.13}_{-0.13}$
	τ		$2.72^{+0.07}_{-0.07}$	$4.49^{+0.05}_{-0.05}$	$4.65^{+0.08}_{-0.08}$	$4.56^{+0.15}_{-0.14}$
Gaussian_0	E_L	keV	$1.017^{+0.013}_{-0.013}$	$0.971^{+0.013}_{-0.013}$	$1.004^{+0.017}_{-0.017}$	$0.987^{+0.024}_{-0.027}$
	σ	keV	$0.096^{+0.013}_{-0.013}$	$0.113^{+0.013}_{-0.012}$	$0.136^{+0.016}_{-0.014}$	$0.118^{+0.029}_{-0.027}$
	EW	eV	150^{+20}_{-19}	49^{+91}_{-15}	103^{+20}_{-20}	105^{+25}_{-24}
Gaussian_1	E_L	keV			$6.394^{+0.013}_{-0.013}$	
	σ	keV			1.3×10^{-2}[a]	
	EW	eV			53^{+41}_{-25}	
Gaussian_2	E_L	keV	$6.672^{+0.017}_{-0.015}$	$6.634^{+0.026}_{-0.023}$	$6.68^{+0.04}_{-0.04}$	$6.67^{+0.04}_{-0.03}$
	σ	keV	$1.27^{+0.02}_{-0.02} \times 10^{-2}$	$0.12^{+0.05}_{-0.05}$	1.3×10^{-2}[a]	$8^{+6}_{-6} \times 10^{-2}$
	EW	eV	995^{+152}_{-143}	186^{+322}_{-27}	281^{+100}_{-49}	528^{+388}_{-156}
Gaussian_3	E_L	keV		$6.966^{+0.030}_{-0.026}$	$6.972^{+0.023}_{-0.019}$	$7.00^{+0.05}_{-0.05}$
	σ	keV		5×10^{-2}[b]	2.3×10^{-2}[a]	1.5×10^{-3}[a]
	EW	eV		75^{+97}_{-20}	167^{+53}_{-40}	169^{+99}_{-89}
Fit quality	χ^2/dof		672/519	840/831	366/317	556/598
	χ^2_{red}		1.30	1.01	1.15	0.93
Energy range		keV	0.3–15.0	0.7–10.0	0.3–15.0	0.3–15

Notes. Our model to fit the spectra: COMPTT+GAUSSIAN_0+GAUSSIAN_1+GAUSSIAN_2+GAUSSIAN_3. Uncertainties at 90% confidence level.
[a] Parameter pegged at hard limit.
[b] Parameter frozen.

We determined the range of physical parameters given by the COMPTT model.

1. The temperature kT_s of the seed photons ranges from 0.056–0.174 keV.
2. The electron temperature kT_e of the Comptonization cloud ranges from 5.99–8.72 keV.
3. The optical depth τ of the Comptonization cloud ranges from 2.65–4.73.

4.2. Chandra Spectral Analysis

The residual broad excess around 1 keV observed in all XMM-Newton spectra was also observed in three out of five HETG/ACIS Chandra spectra analyzed in this paper. This feature and the narrow emission lines (narrow excesses $\gtrsim 2\sigma$) present in the Chandra spectra were modeled by simple Gaussian components. Here U Gem has one HETG/ACIS observation in quiescence and one in the outburst state, whereas SS Cyg was observed once in quiescence and twice in the outburst state.

Fitting the continuum with only one COMPTT component without adding any components to account for the emission lines, the best fit gives a χ^2_{red} of 1.85 (131/71) and 2.57 (321/125) for U Gem ObsIDs 647 and 3767, respectively, and 1.24 (589/478), 2.5 (421/168), and 1.57 (143/91) for SS Cyg ObsIDs 646, 648, and 2307, respectively. When Gaussian components were added to the fit, it led to a χ^2_{red} of 1.03 (67/65) and 1.01 (114/113) for U Gem ObsIDs 647 and 3767, respectively, and 0.97 (453/467), 0.80 (121/151), and 0.64 (52/81) for SS Cyg ObsIDs 646, 648, and 2307, respectively.

Tables 4 and 5 show the best-fit parameters and fit quality for each spectrum of U Gem and SS Cyg, respectively. Figures 3–4 show spectral fits.

In U Gem, the values of the temperature kT_e and τ parameters agree at the 90% confidence level in the two observations: τ is ∼5, and kT_e is equal to $5.0^{+0.5}_{-0.5}$ and 6^{+5}_{-2} keV in ObsIDs 647 (in quiescence) and 3767 (in outburst), respectively. On the other hand, a value of the temperature kT_s of the seed photons in ObsID 3767 ($0.66^{+0.12}_{-0.10}$ keV) appears ∼eight times greater than the temperature in ObsID 647 ($0.66^{+0.12}_{-0.10}$ keV). For the two observations, the total model led to a χ^2_{red} of 1.0 (see Table 4).

In SS Cyg, independent of the source state, the best fits were found in general by a COMPTT component with a kT_s of 0.10 keV, kT_e of ∼5 keV, and τ of ∼6. It is important to stress that initially, all parameters were considered free. However, the electron temperature kT_e appears to be not well constrained by the fits; it assumed values either greater than the upper limit given by the Chandra effective energy band (8 keV) or lower than the minimum value acceptable by the Comptonization model (5 keV; see Hua & Titarchuk 1995). Therefore, this parameter was kept fixed in the three fits. The spectrum of ObsID 648 is the only one that shows a very low seed photon temperature kT_s of $0.020^{+0.004}_{-0.003}$ keV; the presence of many lines in the soft energy band of this spectrum may affect the value of this parameter. We obtained a χ^2_{red} of ∼1.0 for the fit to ObsID 646 and lower than 1.0 for ObsID 648 and 2307 (see Table 5).

The LETG/HRC spectra of SS Cyg and U Gem were not successfully described by only one thermal Comptonization component. Moreover, the presence of many lines in the 0.07–2 keV energy band makes it difficult to satisfactorily fit the data. For example, a good fit in terms of the χ^2 statistic ($\chi^2_{\text{red}} < 2$) is obtained when the soft energy band ($E < 2.5$ keV in SS Cyg and $E < 1.5$ keV in U Gem, respectively) is not taken into account. In this case, fitting SS Cyg and U Gem spectra with a thermal COMPTB component (Farinelli et al. 2008) and two Gaussian components—with centroid energies

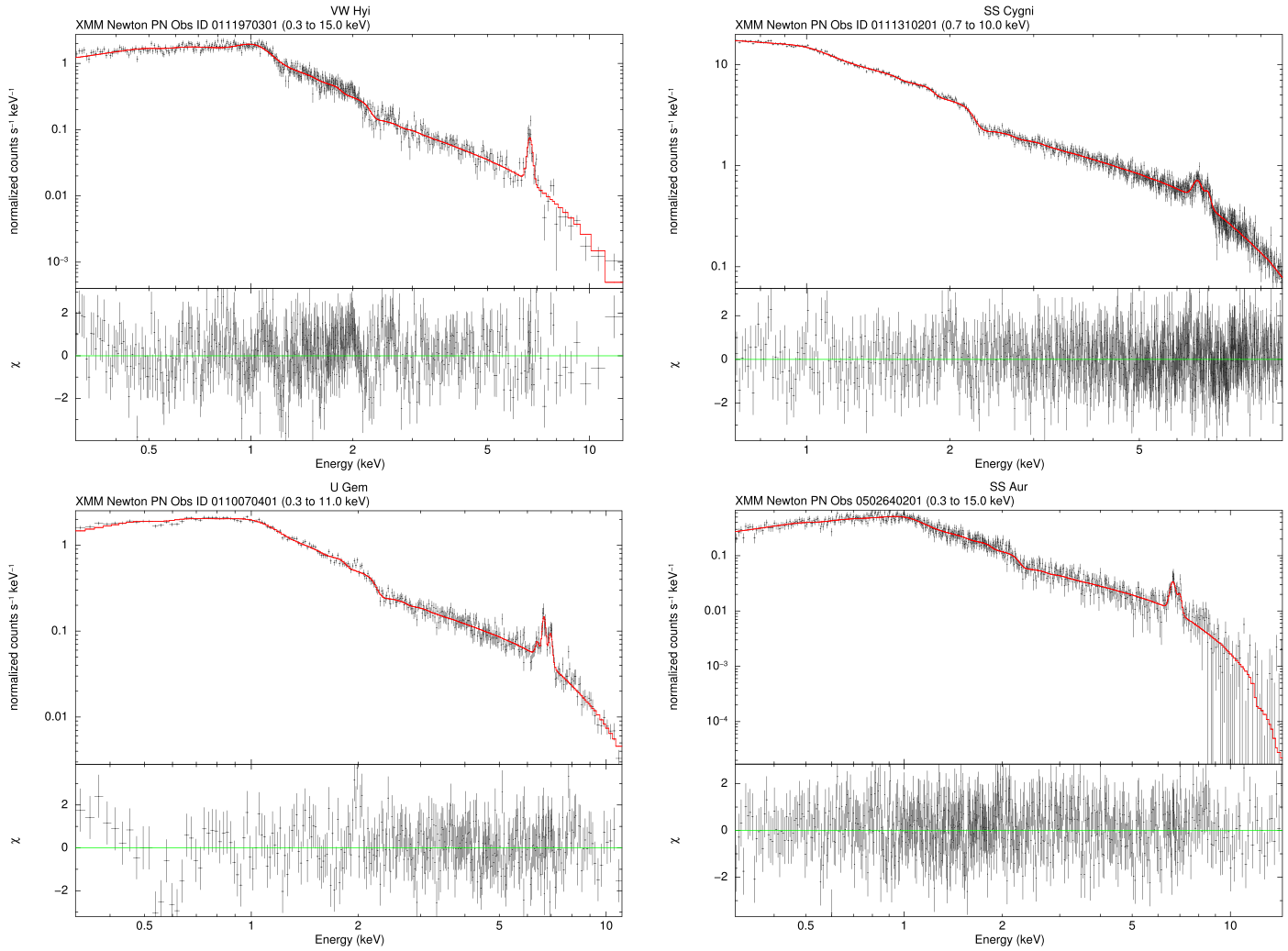

Figure 2. The XMM-Newton EPIC-pn spectra of the four nmCVs analyzed. Top left panel: spectrum of VW Hyi in the 0.3–15.0 keV energy range, data (black) and total model COMPTT+GAUSSIAN+GAUSSIAN (solid red line). Bottom left panel: spectrum of U Gem in the 0.3–15.0 keV energy range, data (black) and best-fit model COMPTT+GAUSSIAN+GAUSSIAN+GAUSSIAN+GAUSSIAN (solid red line). Top right panel: spectrum of SS Cyg in the 0.7–10.0 keV energy range, data (black) and best-fit model COMPTT+GAUSSIAN+GAUSSIAN+GAUSSIAN (solid red line). Bottom right panel: spectrum of SS Aur in the 0.3–15 keV energy range, data (black) and best-fit model COMPTT+GAUSSIAN+GAUSSIAN+GAUSSIAN (solid red line). The bottom panels show the residuals of the data vs. the model.

Table 3
Emission Lines Compatible with the Line Centroid Energy of the Gaussian Component Fit to the Broad Residual Excess (in the 0.8–1.2 keV Energy Range) Present in the Soft X-Ray Spectra of All nmCVs Analyzed

Ion	Transition	Energy (keV)	λ (Å)	DNe
Ne X	1 s—2p	1.022	12.131	VW Hyi, U Gem
Fe XVII	$2p^6\ ^1S - 2p^5 4s^1 P$	0.976	12.703	SS Cyg, SS Aur
	$2p^6\ ^1S - 2p^5 4d^1 P$	1.023	12.119	VW Hyi
Fe XXI	$2s^2 2p^2\ ^3P - 2s2p^2 3p^3 P$	0.992	12.498	SS Aur, U Gem
	$2p^2\ ^3P - 2p3d^3 D$	1.008	12.300	VW Hyi, U Gem, SS Aur

at 1.86 and 2.005 keV—led to a $\chi^2_{\rm red}$ of 1.34 (16/12) and 1.33 (47.9/36), respectively.

4.3. Emission Lines in the HETG/ACIS Spectra

The broad residual excess that peaked at ∼1 keV, observed in all XMM-Newton EPIC-pn spectra, was also observed in the Chandra spectra of U Gem ObsID 3767 in outburst and SS Cyg ObsIDs 648 and 2307 (in outburst). This broad excess could be an emission from Fe XVII, Fe XXI, or Ne X ions (see Table 3). However, the fit of this feature with a Gaussian component led to lower centroid energies. In U Gem ObsID 3767, the Gaussian line energy is frozen at 1.0 keV, with σ equal to $0.24^{+0.07}_{-0.06}$ keV (see Table 4). In SS Cyg ObsIDs 648 and 2307, it is equal to $0.87^{+0.03}_{-0.04}$ and $0.93^{+0.04}_{-0.05}$ keV, respectively, with σ equal to $0.15^{+0.03}_{-0.02}$ and $0.10^{+0.04}_{-0.03}$ keV, respectively (see Table 5). Table 6 summarizes the possible resonance narrow emission lines observed in the Chandra HETG/ACIS spectra. In U Gem (see Table 4), the spectrum of ObsID 647 shows two emission lines with centroid energies at $6.63^{+0.08}_{-0.07}$ (compatible with the He-like K_α Fe line at 6.7 keV) and $2.006^{+0.004}_{-0.001}$ (compatible with

Table 4
Spectral Analysis of the Chandra HETG/ACIS Observations of U Gem Using Pure Thermal COMPTT and Gaussian Components

Component	Parameter	Unit	ObsID 647	ObsID 3767
CompTT	kT_s	keV	$0.087^{+0.004}_{-0.010}$	$0.66^{+0.12}_{-0.10}$
	kT_e	keV	$5.0^{+0.5}_{-0.5}$	6^{+5}_{-2}
	τ		$5.1^{+0.3}_{-0.3}$	5^{+1}_{-1}
Gaussian_0	E_L	keV	$6.63^{+0.08}_{-0.07}$	$6.68^{+0.02}_{-0.02}$
	σ	keV	$0.06^{+0.04}_{-a}$	$0.06^{+0.02}_{-0.02}$
Gaussian_1	E_L	keV	$2.006^{+0.004}_{-0.001}$	$2.004^{+0.001}_{-0.005}$
	σ	keV	$2^{+1}_{-a} \times 10^{-3}$	$9^{+3}_{-3} \times 10^{-3}$
Gaussian_2	E_L	keV		$1.86^{+0.01}_{-0.01}$
	σ	keV		$1.5^{+0.5}_{-0.4} \times 10^{-2}$
Gaussian_3	E_L	keV		1.00[b]
	σ	keV		$0.24^{+0.07}_{-0.06}$
Fit quality	χ^2/dof		67/65	114/113
	χ^2_{red}		1.03	1.01
Energy range		keV	0.4–10	0.4–10

Notes. Uncertainties at 90% confidence level.
[a] Parameter pegged at hard limit.
[b] Parameter frozen.

Si XIV at 2.007 keV) keV. The spectrum of ObsID 3767 shows three more emission lines with centroid energies at $6.68^{+0.02}_{-0.02}$ (compatible with the He-like K_α Fe line), $2.004^{+0.001}_{-0.005}$ (at 3σ of the Si XIV line), and $1.86^{+0.01}_{-0.01}$ (compatible with Si XIII at 1.865 keV) keV.

In SS Cyg (see Table 5), the spectrum of ObsID 646 shows only the three iron lines in the 6.4–7.0 keV energy range: at $6.39^{+0.01}_{-0.01}$ (compatible with the neutral K_α Fe line), $6.67^{+0.01}_{-0.02}$ (at 3σ of the He-like K_α Fe line), and $6.97^{+0.01}_{-0.03}$ (at 3σ of the H-like K_α Fe line) keV. The spectrum of ObsID 648 shows a total of six emission lines with centroid energies at $0.87^{+0.03}_{-0.04}$ (compatible with emission from either Ca XVIII, Fe XVII, Ni XIX, or Ni XVIII; see Table 6), $1.346^{+0.004}_{-0.004}$ (compatible with emission from Mg XI at 1.343 and 1.5σ from the 1.352 keV line), $1.473^{+0.004}_{-0.005}$ (compatible with emission from Mg XII at 1.473), $1.859^{+0.003}_{-0.004}$ (at 2σ of Si XIII emission), $2.005^{+0.003}_{-0.004}$ (compatible with Si XIV emission), and $6.65^{+0.03}_{-0.04}$ (at 1.7σ from the He-like K_α Fe line) keV. The spectrum of ObsID 2307 shows a total of four emission lines with centroid energies at $0.93^{+0.04}_{-0.05}$ (compatible with Ca XVIII, Ni XIX, and Ne IX), $1.472^{+0.008}_{-0.007}$ (compatible with Mg XII), $1.857^{+0.005}_{-0.005}$ (at 1.6σ from the Si XIII line), and $6.61^{+0.01}_{-0.01}$ (at 1.7σ from the Fe XXII K_α line at 6.627 keV) keV; see Table 6.

4.4. RXTE Spectral Analysis

Almost all observations showed a low count rate (<1 counts s^{-1}) in the energy band >25 keV of the PCA spectra. The same, or no counts, was observed in the 40–150 keV of the HEXTE spectra. Therefore, except for ObsID 50012-01-01-00 of SS Cyg, we performed the spectral analysis considering only the PCA spectra with an energy range up to 25 keV.

Because RXTE ObsID 50012-01-01-00 of SS Cyg is simultaneous with Chandra ObsID 646, we have analyzed the 0.4–8 keV HETG/ACIS Chandra spectral band together with the 8–60 keV PCA and 60–150 keV HEXTE energy band of RXTE.

The spectra of U Gem ObsID 80011-01-02-00, SS Aur ObsID 30026-03-01-00, and SS Cyg ObsID 10040-01-01-000 were well described in the ~5–25 keV energy band by only one COMPTT component. On the other hand, the other three spectra of SS Cyg (ObsIDs 50012-01-01-00, 10040-01-01-001, and 10040-01-01-00) required a second spectral component. For these three observations, we fit a model consisting of (1) a blackbody (BBODY) plus a Comptonization (COMPTT) component or (2) a sum of two Comptonization (COMPTT) components.

In general, taking into account the χ^2 statistic and the range of physical parameters, the best fits were found for the second case—that is, when two COMPTT components were used to describe the total spectra. Namely, the best fits were found when both the electron temperature kT_e and the optical depth τ of the COMPTT model were tied between the two components. Figure 5 shows the geometry of our Comptonization model. We definitely establish that there is a disk that supplies the seed photons for the TL (Compton cloud). Red lines indicate the trajectories of the photons that illuminate the TL coming from the WD surface. As a result, the emergent X-ray spectrum formed in the TL as a result of upscattering of the seed photons of the disk and WD surface off hot electrons of the Compton cloud.

In order to assess the statistical significance of the second COMPTT component, we computed the probability of chance improvement of the χ^2 by means of an F-test. It is worth stressing that the F-test to be used in this case is not the one that uses the $\Delta\chi^2$ as test statistics (let us call it an independent F-test, or I–F-test). Indeed, in order to correctly use the I–F-test, the χ^2 variables must be linearly independent. In our case, the two components share some parameters and therefore are not independent by construction. Thus, we must use another test statistics: the dependent F-test (D–F-test). This test statistics is defined in terms of the ratio between the normalized χ^2 (see, e.g., Barlow 1989; Press et al. 1992) and has already been successfully used for the assessment of the statistical significance of multiplicative components (that are also dependent components by construction) by Orlandini et al. (2012) and Iyer et al. (2015), among others.

The probability of chance improvement of the χ^2 by adding the second COMPTT component, evaluated by means of a *D–F*-test, is equal to 3×10^{-8} in SS Cyg ObsID 50012-01-01-00, 0.07 in ObsID 10040-01-01-001, and 0.02 in ObsID 10040-01-01-00.

From these values, we see that the second COMPTT component is statistically significant (equivalent to 5.4σ for a one-tailed test) only for the ObsID 50012-01-01-00 SS Cyg observation. This does not mean that this component is not also present in the other two RXTE observations but only that the signal-to-noise ratio in the latter two observations does not allow its detection above a confidence level of about 2σ.

Table 7 shows the best-fit parameters and fit quality for each source and observation. Figure 6 shows the spectral fits to U Gem and SS Aur. Figure 7 shows the spectral fits to the three observations of SS Cyg in outburst. It is important to stress that these three observations are consecutive. Figure 8 shows the spectral fit to the 0.4–150 keV simultaneous Chandra/RXTE spectra of SS Cyg in quiescence. Finally, Figure 9 shows the photon index Γ as a function of the best-fit electron temperatures kT_e of the TL for all sources analyzed using our nmCV sample.

Table 5
Spectral Analysis of the Chandra HETG/ACIS Observation of SS Cyg Using Thermal COMPTT and Gaussian Components

Component	Parameter	Unit	ObsID 646	ObsID 648	ObsID 2307
CompTT	kT_s	keV	$0.10^{+0.05}_{-a}$	$0.020^{+0.004}_{-0.003}$	$0.11^{+0.01}_{-0.01}$
	kT_e	keV	5.0[b]	5.0[b]	5.0[b]
	τ		$5.9^{+0.1}_{-0.1}$	$7.2^{+0.3}_{-0.3}$	$5.7^{+0.3}_{-0.3}$
Gaussian_0	E_L	keV		$0.87^{+0.03}_{-0.04}$	$0.93^{+0.04}_{-0.05}$
	σ	keV		$0.15^{+0.03}_{-0.02}$	$0.10^{+0.04}_{-0.03}$
Gaussian_1	E_L	keV		$1.346^{+0.004}_{-0.004}$	
	σ	keV		$1.09^{+0.6}_{-0.3} \times 10^{-2}$[a]	
Gaussian_2	E_L	keV		$1.473^{+0.004}_{-0.005}$	$1.472^{+0.008}_{-0.007}$
	σ	keV		$1.2^{+0.4}_{-0.3} \times 10^{-2}$[a]	$1.0^{+0.8}_{-0.6} \times 10^{-2}$
Gaussian_3	E_L	keV		$1.859^{+0.003}_{-0.004}$	$1.857^{+0.005}_{-0.005}$
	σ	keV		$1.3^{+0.3}_{-0.2} \times 10^{-2}$	$1.4^{+0.4}_{-0.3} \times 10^{-2}$
Gaussian_4	E_L	keV		$2.005^{+0.003}_{-0.004}$	
	σ	keV		$1.3^{+0.3}_{-0.3} \times 10^{-2}$[a]	
Gaussian_5	E_L	keV	$6.39^{+0.01}_{-0.01}$	$6.65^{+0.03}_{-0.04}$	$6.61^{+0.01}_{-0.01}$
	σ	keV	0.02[b]	$0.08^{+0.08}_{-0.09}$	0.02[b]
Gaussian_6	E_L	keV	$6.67^{+0.01}_{-0.02}$		
	σ	keV	0.03[b]		
Gaussian_7	E_L	keV	$6.97^{+0.01}_{-0.03}$		
	σ	keV	0.02[b]		
Fit quality	χ^2/dof		453/467	121/151	52/81
	χ^2_{red}		0.97	0.80	0.64
Energy range		keV	0.4–8.0	0.4–10	0.4–10

Notes. Uncertainties at 90% confidence level.
[a] Parameter pegged at hard limit.
[b] Parameter frozen.

Because of the low energy resolution of the PCA, the emission iron lines expected in the ∼6.4–7.0 keV energy range are not well resolved. Therefore, only one Gaussian component is required to account for the excesses in this energy range. Table 8 shows the line energy found for each observation, wherein for the simultaneous Chandra/RXTE spectra, as an exception, we show the three iron emission lines observed by HETG/ACIS Chandra.

5. The TL in a WD and Spectral Index of the Expected Emergent Spectrum in the Comptonization Scenario

As Farinelli & Titarchuk (2011, hereafter FT11) pointed out, the energy release in the TL of an NS determines the spectral index of the emergent spectrum. In similar way, we use the TL model to estimate the index for the case of a WD. But in this case, instead of the reflection inner boundary of the TL at an NS, we use the pure absorption boundary at a WD. It was demonstrated by FT11 that the energy flux per unit surface area of the TL (corona) can be found as

$$Q_{\rm cor} = 20.2 \int_0^{\tau_0} \varepsilon(\tau) T_e(\tau) d\tau, \quad (1)$$

where $T_e(\tau)$, $\varepsilon(\tau)$, and τ_0 are the plasma (electron) temperature, the radiation density distribution in the TL, and its Thomson optical depth, respectively.

We obtain the energy distribution $\varepsilon(\tau)$ as a solution of the diffusion equation

$$\frac{d^2\varepsilon}{d\tau^2} = -\frac{3Q_{\rm cor}}{c\tau_0}, \quad (2)$$

where c is the speed of light.

We should also add the two boundary conditions at the inner TL boundary, which can be an absorbed surface at WD $\tau = \tau_0$, and the outer boundary $\tau = 0$. They are, respectively,

$$\frac{d\varepsilon}{d\tau} + \frac{3}{2}\varepsilon|_{\tau=\tau_0} = 0, \quad (3)$$

$$\frac{d\varepsilon}{d\tau} - \frac{3}{2}\varepsilon|_{\tau=0} = 0. \quad (4)$$

We find the solution $\varepsilon(\tau)$ of Equations (2)–(4):

$$\varepsilon(\tau) = \frac{Q_{\rm cor}}{c}\{1 + 3/2\ \tau_0[(\tau/\tau_0) - (\tau/\tau_0)^2]\}\ . \quad (5)$$

Thus, integration of $\varepsilon(\tau)$ gives us

$$\int_0^{\tau_0} \varepsilon(\tau) d\tau = \frac{Q_{\rm cor}}{c}\tau_0(1 + \tau_0/4). \quad (6)$$

Now we can estimate the Comptonization Y-parameter in the TL using Equations (1) and (6). We rewrite Equation (1) using the mean value theorem as

$$Q_{\rm cor} = 20.2\hat{T}_e \int_0^{\tau_0} \varepsilon(\tau) d\tau, \quad (7)$$

where $\hat{T}_e$ is the mean electron temperature in the TL.

Substitution of Equation (6) into Equation (7) leads to the following estimate (Y-parameter) in the TL (see a definition of Y-parameter in Rybicki & Lightman 1979):

$$\frac{k\hat{T}_e\tau_0(\tau_0/4 + 1)}{m_e c^2} = 0.25. \quad (8)$$

As we can see in Figure 9, the photon index Γ shows only small deviations from 1.8; namely, for most of our sources, $\Gamma = 1.8 \pm 0.1$, while the Compton cloud electron temperature

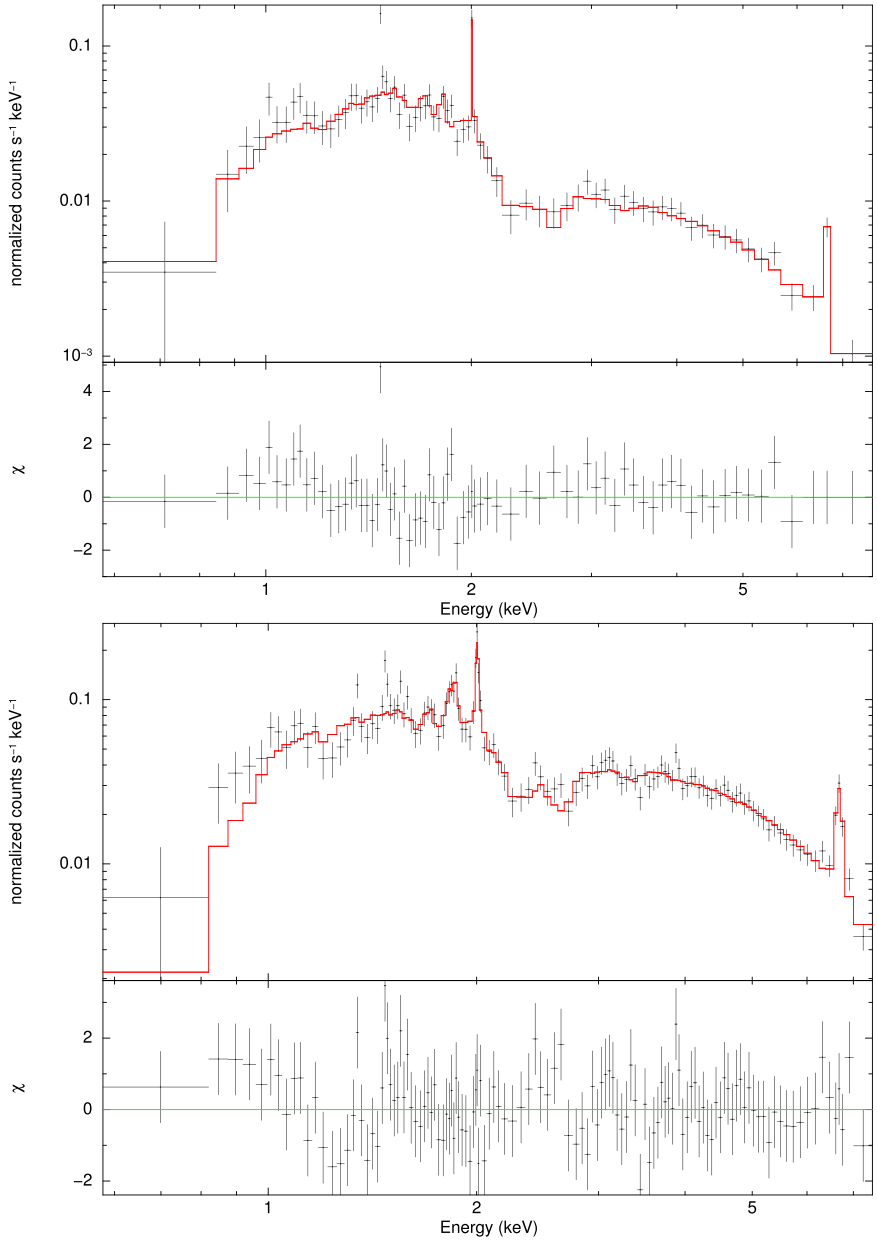

Figure 3. Chandra HETG/ACIS spectra of U Gem in the 0.4–10 keV energy range. Top panel: spectral fit to ObsID 647 (see Table 4, fourth column), data (black) and total model COMPTT+GAUSSIAN+GAUSSIAN (solid red line). Bottom panel: spectral fit to ObsID 3767 (see Table 4, fifth column), data (black) and best-fit model COMPTT+GAUSSIAN+GAUSSIAN+GAUSSIAN+GAUSSIAN components (solid red line). The bottom panels show the residuals of the data vs. the model.

varies from 5 to 45 keV. In some sense, this index behavior is similar to that observed in NSs (Titarchuk et al. 2014).

As already pointed out in classical work (FT11), spectral formation in plasma clouds of finite size (bounded medium) is related to the distribution law of the number of scatterings that seed photons experience before their escape. If u_{av} denotes the average number of photon scatterings, and the dimensionless scattering number is $u = N_e \sigma_T c t$, then the distribution law for $u \gg u_{av}$ is given by (Sunyaev & Titarchuk 1980, 1985)

$$P(u) = A(u, \tau_0) e^{-\beta u}. \quad (9)$$

For a diffusion regime when $\tau_0 > 1$, the corresponding $\beta = \lambda_1^2/3$, where λ_1 is the first eigenvalue of the diffusion space operator. As reported in Sunyaev & Titarchuk (1985), the eigenvalue problem for photon diffusion in a slab with total optical depth τ_0 is derived from a solution of the differential equation for the zero-moment intensity,

$$\frac{d^2 J}{d\tau^2} + \lambda^2 J = 0, \quad (10)$$

with boundary conditions $dJ/d\tau - (3/2)J = 0$ and $dJ/d\tau + (3/2)J = 0$ for $\tau = 0$ and τ_0, respectively. This leads to the transcendental equation for the eigenvalue λ_n, $n = 1, 2, 3 \ldots$,

$$\tan(\lambda_n \tau_0/2) = \frac{2}{3\lambda_n}, \quad (11)$$

which has a solution for $n = 1$,

$$\lambda_1 = \frac{\pi}{2(\tau_0/2 + 2/3)}. \quad (12)$$

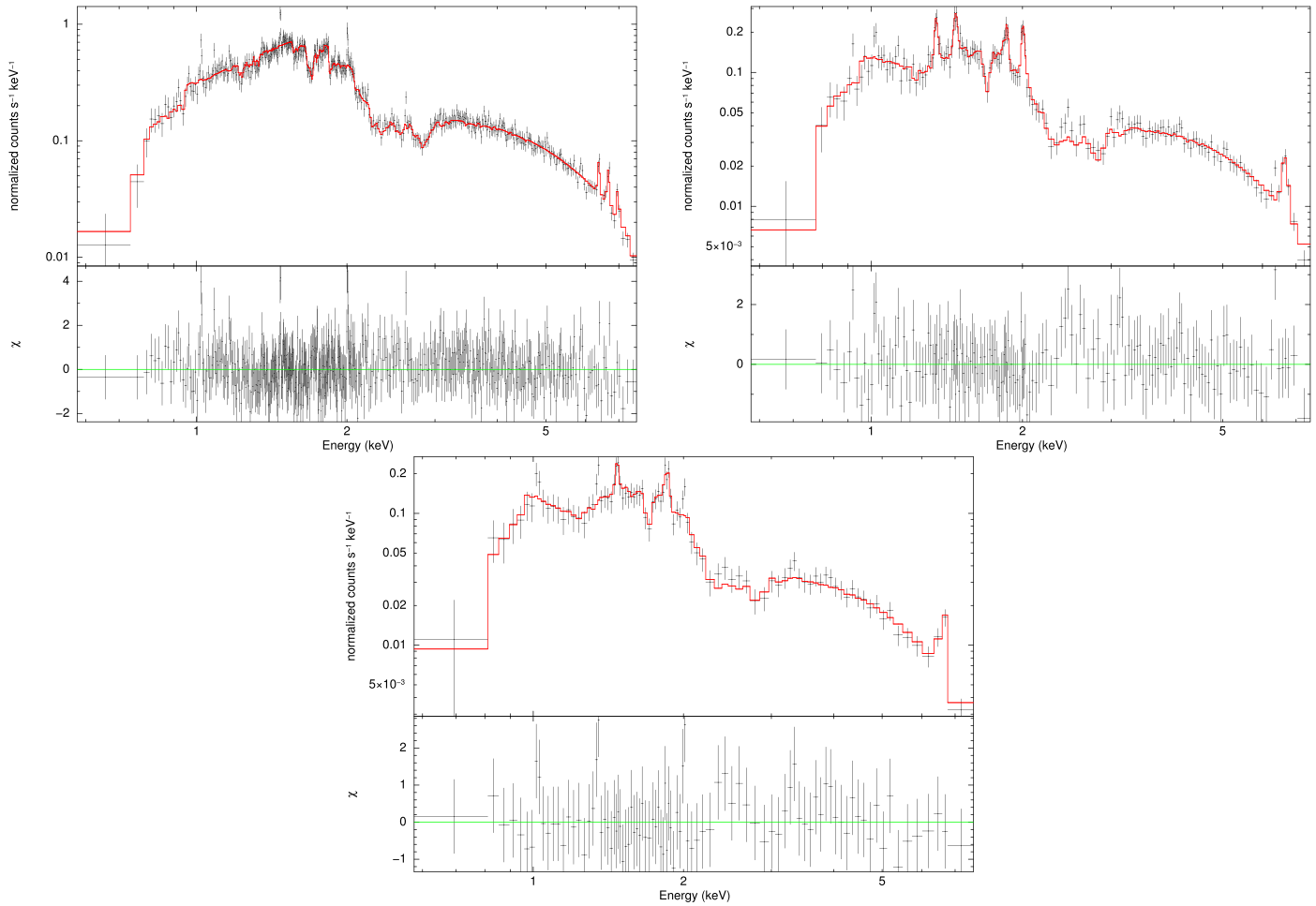

Figure 4. Chandra HETG/ACIS spectra of SS Cyg in the 0.4–10 keV energy range. Top left panel: spectral fit to ObsID 646 (see Table 5, fourth column), data (black) and total model COMPTT+GAUSSIAN+GAUSSIAN+GAUSSIAN (solid red line). Top right panel: spectral fit to ObsID 648 (see Table 5, fifth column), data (black) and best-fit model COMPTT+GAUSSIAN+GAUSSIAN+GAUSSIAN+GAUSSIAN+GAUSSIAN+GAUSSIAN (solid red line). Bottom panel: spectral fit to ObsID 2307 (see Table 5, sixth column), data (black) and total model COMPTT+GAUSSIAN+GAUSSIAN+GAUSSIAN (solid red line). The bottom panels show the residuals of the data vs. model.

Table 6
X-Ray Lines, Other than the Iron Lines Expected in the 6.4–7.0 keV Energy Range, Compatible with the Centroid Energy of a Gaussian Component Present in the Chandra HETG/ACIS Spectra

Ion	Transition	Energy (keV)	λ (Å)	DNe	ObsID
Ca XVIII	$2s - 4p$	0.886	13.993	SS Cyg	648, 2307
Fe XVII	$2s^6 - 2p^5 3d\,^1P$	0.826	15.010	SS Cyg	648
Ni XIX	$2p^6 - 2p^5 3s\,^3P$	0.884	14.025	SS Cyg	648, 2307
Ni XVIII	$2s^6 - 3s^2S - 2p^5 3s^2\,^2P$	0.879	14.105	SS Cyg	648
Ne IX	$1s^2\,^1S - 1s2p\,^1P$	0.921	13.461	SS Cyg	2307
Mg XI	$1s^2\,^1S - 1s2p\,^3P$	1.343	9.232	SS Cyg	648
Mg XI	$1s^2\,^1S - 1s2p\,^1P$	1.352	9.170	SS Cyg	648
Mg XII	$1s - 2p$	1.473	8.417	SS Cyg	648, 2307
Si XIII	$1s^2\,^1S - 1s2p\,^1P$	1.865	6.648	U Gem	3767
				SS Cyg	648, 2307
Si XIV	$1s - 2p$	2.007	6.177	U Gem	647, 3767
				SS Cyg	648
Fe XXII	K_α	6.627	1.871	SS Cyg	2307

But the spectral index α (photon index $\Gamma = \alpha + 1$) is

$$\alpha = -3/2 + (9/4 + \beta/\theta)^{1/2}, \quad (13)$$

where $\beta = \lambda_1^2/3$ and $\theta = kT_e/(m_e c^2)$ (Sunyaev & Titarchuk 1980). Thus,

$$\alpha = -3/2 + (9/4 + \pi^2/[12(\tau_0/2 + 2/3)^2\theta]^{1/2}, \quad (14)$$

and, using Equation (8), we obtain that $\alpha \lesssim 0.85$ (or $\Gamma \lesssim 1.85$). This is precisely what we observed (see Figure 9).

6. Discussion

As previously mentioned, the Comptonization model is not the standard radiative one currently used for the description of

Table 7
Spectral Analysis of RXTE Observations Using Thermal COMPTT Component(s)

ObsID			U Gem 80011-01-02-00	SS Aur 30026-03-01-00	SS Cyg 50012-01-01-00	SS Cyg 10040-01-01-000	SS Cyg 10040-01-01-001	SS Cyg 10040-01-01-00
State			Outburst	Quiescence	Quiescence[b]	Outburst	Outburst	Outburst
Component	Parameter	Unit						
CompTT$_1$	kT_{s1}	keV	$0.23^{+0.03}_{-0.03}$	$0.05^{+0.01}_{-0.01}$	$0.11^{+0.06}_{-a}$	$0.20^{+0.01}_{-0.01}$	$0.31^{+0.05}_{-0.05}$	$0.29^{+0.03}_{-0.03}$
	kT_{e1}	keV	43^{+5}_{-4}	37^{+6}_{-5}	$32.8^{+0.5}_{-0.6}$	25^{+1}_{-1}	$5.3^{+0.3}_{-0.3}$	$5.4^{+0.3}_{-0.3}$
	τ_1		$0.83^{+0.26}_{-0.16}$	$1.0^{+0.1}_{-0.1}$	$1.21^{+0.01}_{-0.01}$	$1.82^{+0.06}_{-0.06}$	$4.8^{+0.2}_{-0.2}$	$4.5^{+0.2}_{-0.2}$
	Norm$_1$		$4^{+1}_{-1} \times 10^{-4}$	$8^{+1}_{-1} \times 10^{-4}$	$3.65^{+0.04}_{-0.04} \times 10^{-3}$	$1.02^{+0.03}_{-0.03} \times 10^{-3}$	$4^{+18}_{-1} \times 10^{-3}$	$8.1^{+0.7}_{-0.7} \times 10^{-3}$
CompTT$_2$	kT_{s2}	keV			$0.89^{+0.02}_{-0.02}$		$0.65^{+0.03}_{-0.03}$	$0.76^{+0.04}_{-0.04}$
	kT_{e2}	keV			$= kT_{e1}$		$=kT_{e1}$	$= kT_{e1}$
	τ_2				$= \tau_1$		$= \tau_1$	$= \tau_1$
	Norm$_2$				$5.0^{+0.1}_{-0.1} \times 10^{-4}$		$3^{+3}_{-2} \times 10^{-3}$	$2^{+3}_{-1} \times 10^{-3}$
Fit quality	χ^2/dof		38/36	40/53	503/554	42/46	42/44	50/44
	χ^2_{red}		1.06	0.88	0.91	0.91	0.94	1.13
Energy range		keV	5–25	2.5–25	0.4–150	2.5–25	2.5–25	2.5–25

Notes. Uncertainties at 90% confidence level. The respective emission lines present in the spectra are presented in Table 8.
[a] Parameter pegged at hard limit.
[b] Simultaneous RXTE/Chandra observation.

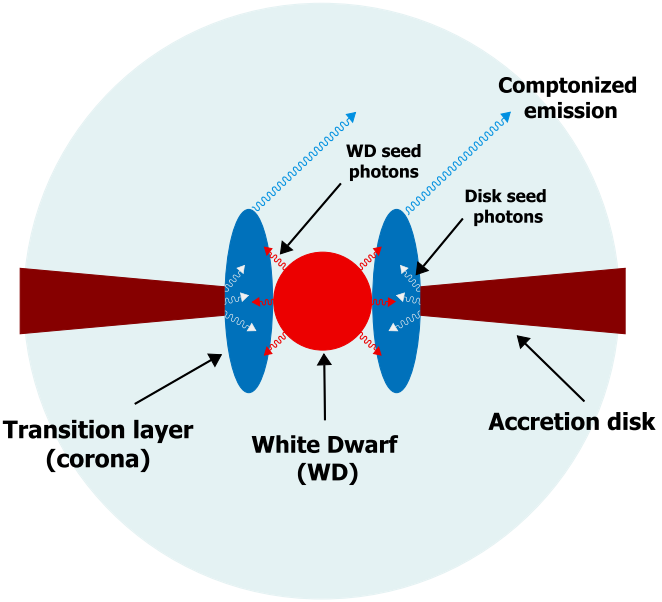

Figure 5. Geometry of the Comptonization framework in nmCVs. The seed photons coming both from the inner part of the accretion disk and from (or close to) the WD surface are upscattered by thermal electrons present in the TL (or corona), which is located between the WD surface and the accretion disk. The light blue sphere around the system represents the region wherein relatively cold material is outflowing, where lines are formed.

the continuum in nmCVs. On the other hand, the Comptonization model is the standard one for fitting the LMXB spectra.

Considering that nmCVs share similarities with LMXBs—that is, they have an accretion disk, a compact object, and a TL (corona, the presence of which is evident from observation of noneclipsed UV emission lines in eclipsing systems; see, e.g., Warner 1995; Mauche & Raymond 2000)—we look for spectral similarities between these two types of X-ray binaries. That is, our main goal is to seek a common physical process that can describe the continuum of both nmCVs and LMXBs.

Figure 5 represents the Comptonization framework in nmCVs, in which the emission lines are produced far from the most central part of the system, where the X-ray continuum is produced.

Because of the broad spectral X-ray energy band of the PCA and HEXTE instruments, we have also analyzed some of the RXTE observations of our source sample, which are available in the archive (see Table 1), including a simultaneous 0.4–150 keV Chandra/RXTE spectrum of SS Cyg in the quiescent state. The broadband, including harder (>15 keV) X-rays, can provide a better understanding of this scenario and the physical parameters in terms of the Comptonization framework in these sources—mainly the electron temperatures and spectral indices.

All sources in our sample were observed in the quiescent state by XMM-Newton EPIC-pn. We found that only one thermal Comptonization component plus Gaussian components successfully fit the XMM-Newton EPIC-pn spectra of two nmCVs: SS Cyg and SS Aur. In terms of χ^2 statistics, our model did not provide a perfect description of the VW Hyi and U Gem XMM-Newton total spectra. In these two cases, the value of χ^2 exceeds the critical value at a 0.01 level of significance. However, the spectral analyses of U Gem using Chandra and RXTE data show a satisfactory fit (see fourth column of Tables 4 and 7). It is likely that the presence of several emission lines, besides the iron complex, in the XMM-Newton spectra of VW Hyi and U Gem worsened the fit quality.

It is important to emphasize that all XMM-Newton spectral fits show best-fit parameters with a mean seed photon temperature $\langle kT_s \rangle$ of 0.14 ± 0.01 keV, a mean optical depth $\langle \tau \rangle$ of 4.1 ± 0.5, and a mean electron temperature $\langle kT_e \rangle$ of 7.2 ± 0.6 keV. The spectral fits performed in the 1.5–15 keV energy range of the XMM-Newton spectra do not allow accurate estimates of the temperature of the seed photons. In this case, the parameters appeared with mean values of $\langle kT_s \rangle$ of 0.25 ± 0.05 keV, $\langle \tau \rangle$ of 4.5 ± 0.5 keV, and $\langle kT_e \rangle$ of 5.9 ± 0.5 keV. Therefore, we obtained a better description of the seed photon temperature when considering the total EPIC-pn spectral band in our analyses.

The Chandra HETG/ACIS spectra show parameters similar to those found by XMM-Newton, with a mean $\langle kT_s \rangle$ of

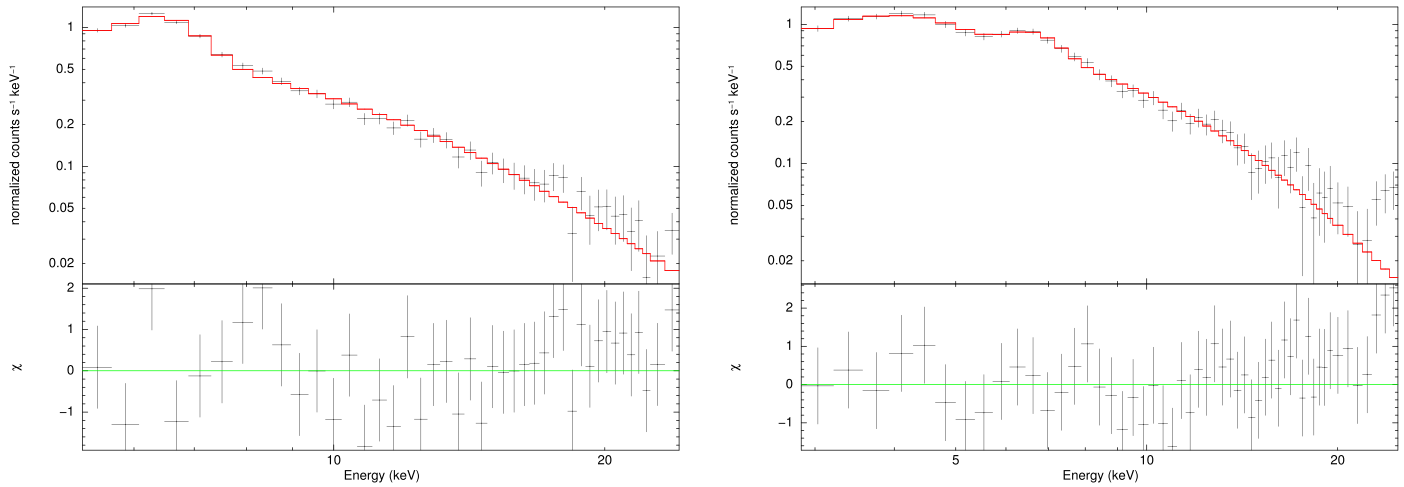

Figure 6. Spectral fits of the RXTE/PCA data for U Gem in outburst (left panel) and SS Aur in quiescence (right panel). The solid red line shows the total COMPTT +GAUSSIAN model (see Tables 7 and 8). The lower panels show the residuals of the data vs. model.

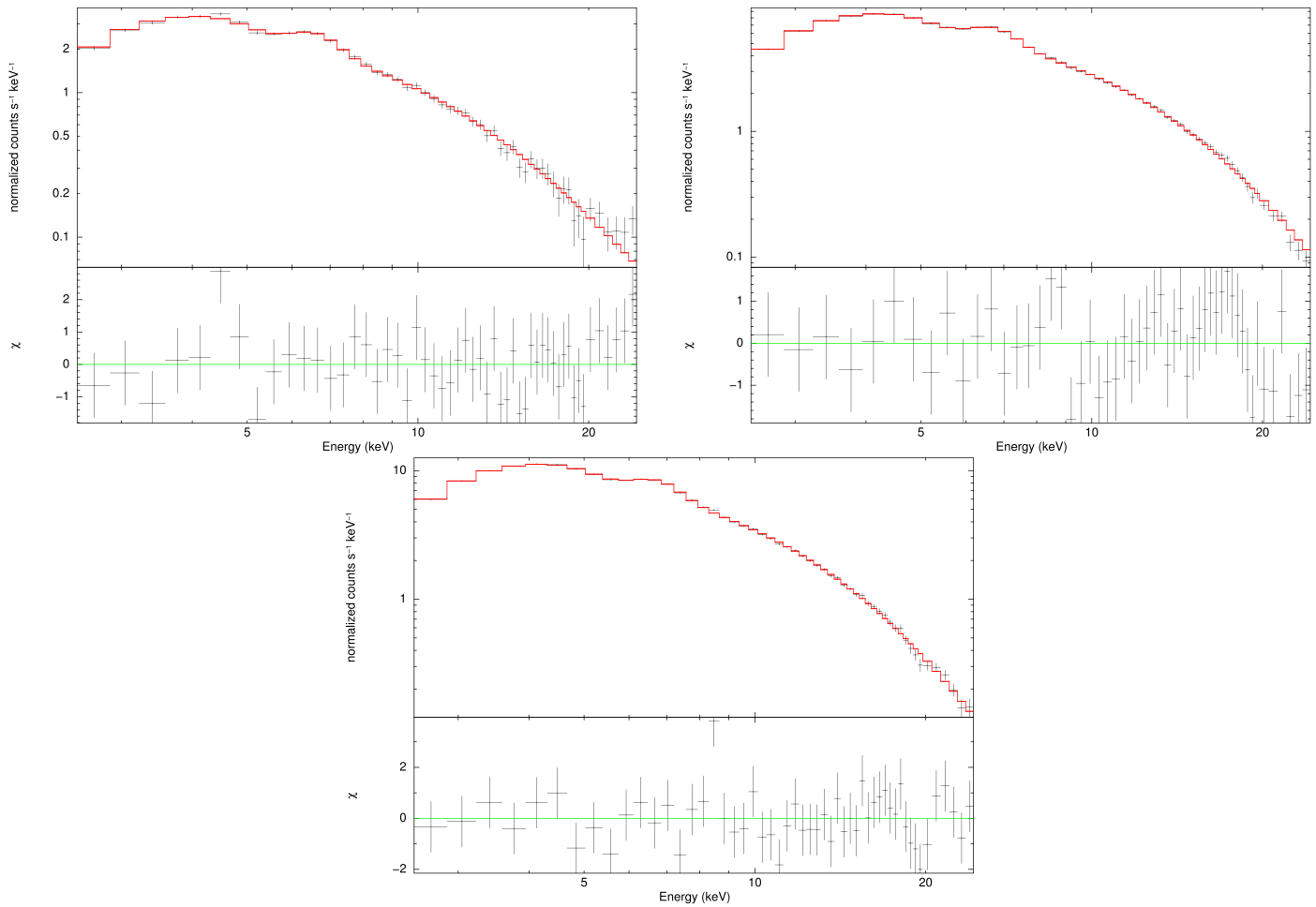

Figure 7. Spectral fits to the RXTE/PCA spectra of SS Cyg in outburst: ObsIDs 10040-01-01-000 (top left panel), 10040-01-01-001 (top right panel), and 10040-01-01-00 (bottom panel). The solid red line shows the COMPTT+GAUSSIAN total model in ObsID 10040-01-01-000 and COMPTT+COMPTT+GAUSSIAN in ObsIDs 10040-01-01-001 and 10040-01-01-00 (see Tables 7 and 8). The lower panels show the residuals of the data vs. model.

0.20 ± 0.12 keV, a mean optical depth $\langle \tau \rangle$ of 5.2 ± 0.2, and a mean temperature $\langle kT_e \rangle$ of 5.8 ± 0.4 keV. Chandra observed SS Cyg once in the quiescent state and twice in the outburst state. We did not obtain a perfect fit for the two observations in outburst (see Table 5). In addition, we did not observe a difference in the spectral continuum parameters between the two states. This can be due to the Chandra effective energy band (<8 keV). Namely, we found that the electron temperature in the Chandra spectra is not very well constrained by these fits.

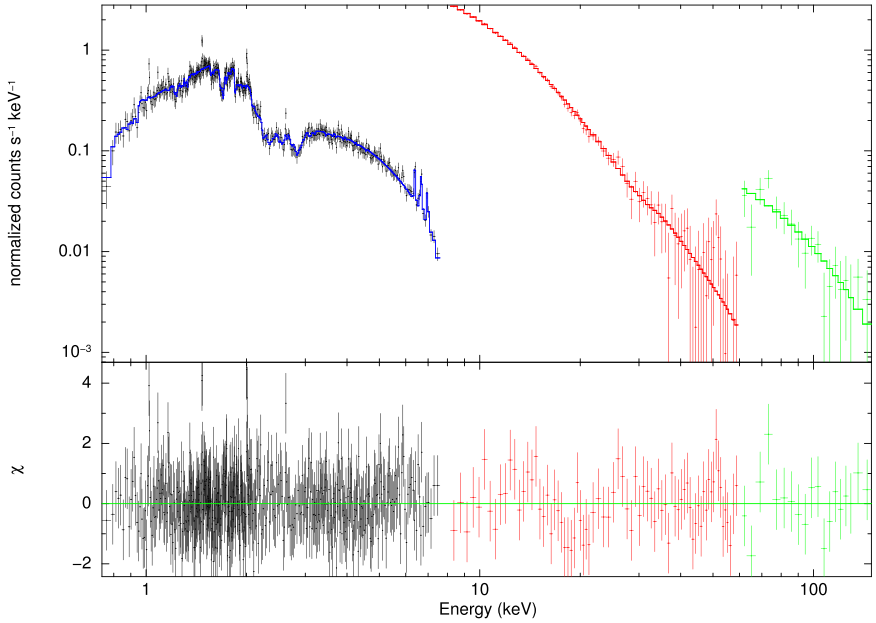

Figure 8. Spectral fit to the simultaneous Chandra/RXTE (ObsID 646/ObsID 50012-01-01-00) spectra of SS Cyg using the COMPTT+COMPTT+GAUSSIAN +GAUSSIAN+GAUSSIAN total model. The black, red, and green points correspond to 0.4–8.0 keV HETG/ACIS, 8.0–60 keV PCA, and 60–150 keV HEXTE data, respectively. The blue, red, and green lines correspond to the best spectral fit (see sixth column of Tables 7 and 8). The lower panel shows the residuals of the data vs. model.

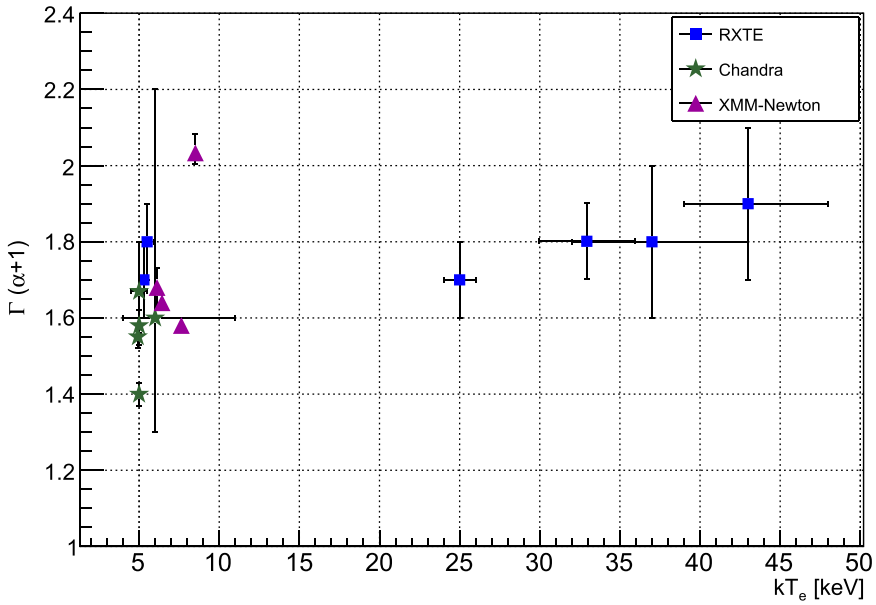

Figure 9. Photon indices Γ vs. the best-fit electron temperatures kT_e in the Compton cloud (TL). Blue, green, and magenta points correspond to analyzed RXTE, Chandra, and XMM-Newton spectra, respectively (see Tables 2, 4, 5, and 7).

In the analyses of the RXTE spectra, a second Comptonization component was necessary for the description of the total spectrum in three observation of SS Cyg. In these cases, a satisfactory spectral fit was found if both kT_e and the optical depth τ of the COMPTT model were tied between the two components. Namely, it means that the total ∼0.4–150 or 2.5–25 keV spectra of all analyzed nmCVs are characterized by only one spectral index α ($\alpha = \Gamma - 1$).

The RXTE spectra of our sample showed a wide range of electron temperatures kT_e in the 5–48 keV range. When one compares the values of α (or Γ) between the different sources (see Table 7 and Figure 9), one does not find any correlation of kT_e with Γ. It is also worth noting that SS Cyg shows $kT_e \sim 5$ keV in outburst, U Gem shows kT_e of 43^{+5}_{-4} keV in outburst, and SS Aur shows a temperature of 37^{+6}_{-5} keV in the quiescent state. Therefore, we establish that we do not find any correlation of kT_e with the spectral state using the data of our set of CVs. For the sake of comparison, we present in Table 9 the best-fitting plasma temperature found by our analyses together with the ones reported by some previous spectral modeling for all CVs in our sample (see Section 2). As shown in Table 9, the spectral modeling present in the literature is not homogeneous, and no clear correlation of plasma temperature with spectral stage is found between the sources in previous spectral modeling as well.

Table 8
Spectral Analysis of the RXTE Observations: Gaussian Component(s)

			U Gem	SS Aur	SS Cyg	SS Cyg	SS Cyg	SS Cyg
ObsID			80011-01-02-00	30026-03-01-00	50012-01-01-00	10040-01-01-000	10040-01-01-001	10040-01-01-00
State			Outburst	Quiescence	Quiescence[b]	Outburst	Outburst	Outburst
Component	Parameter	Unit						
Gaussian_1	E_{L1}	keV	$6.54^{+0.05}_{-0.06}$	$6.63^{+0.14}_{-0.13}$	$6.39^{+0.01}_{-0.01}$	$6.68^{+0.09}_{-0.09}$	$6.64^{+0.03}_{-0.03}$	$6.64^{+0.03}_{-0.03}$
	σ_{L1}	keV	$0.36^{+0.05}_{-0.06}$	$0.32^{+0.19}_{-a} \times 10^{-2}$	$1.8^{+1.1}_{-1.7} \times 10^{-2}$	$0.38^{+0.12}_{-0.12}$	$0.33^{+0.05}_{-0.05}$	$0.33^{+0.04}_{-0.04}$
Gaussian_2	E_{L2}	keV			$6.67^{+0.01}_{-0.02}$			
	σ_{L2}	keV			$3.4^{+1.6}_{-1.1} \times 10^{-2}$			
Gaussian_3	E_{L3}	keV			$6.97^{+0.01}_{-0.02}$			
	σ_{L3}	keV			$2.12^{+0.02}_{-a} \times 10^{-2}$			

Notes. Uncertainties at 90% confidence level.
[a] Parameter pegged at hard limit.
[b] Simultaneous Chandra/RXTE (ObsID 646/50012-01-01-00) spectra. The lines present in the HETG/ACIS Chandra spectrum are shown.

In the RXTE spectra, the first Comptonization component shows a mean value of the seed photon temperature kT_{s1} of 0.20 ± 0.04 keV. This temperature appears higher in the observations in outburst. When in outburst, SS Cyg shows $kT_{s1} \sim 2$–3 times higher. It is important to point out, however, that the RXTE data do not precisely determine the seed photon temperatures if their values are much less than 1 keV because the lower limit of the RXTE data is ~3 keV. Therefore, all values of the seed photons kT_s obtained through RXTE data (see Table 7) are upper limits.

In the three RXTE observations of SS Cyg for which the second Comptonization component was required, the seed photon temperature kT_{s2} of the second component appears with a mean value of 0.77 ± 0.07 keV. This component is not observed at the very early stage of the optical outburst but reappears in the consecutive observations, increasing its value to $0.76^{+0.04}_{-0.04}$ keV in the last observation, closer to the outburst optical peak. In the observation of the quiescent state, kT_{s2} is equal to $0.89^{+0.02}_{-0.02}$ keV. Therefore, we did not observe a huge difference in the temperature kT_{s2} between the different states. Interestingly, the Chandra spectrum of U Gem ObsID 3767 in outburst (see Table 4) shows a single Comptonization component with a seed photon temperature of $0.66^{+0.12}_{-0.10}$ keV. A transient hard component was reported in U Gem during its 2004 outburst (see Section 2.1 and Güver et al. 2006) and associated with the outburst state. On the other hand, we also observed this hard component during the quiescent state in SS Cyg. This is evidence that this hard X-ray component is not a spectral feature of outburst states only.

In the Comptonization framework, the seed photons are upscattered (Comptonized) by hot electrons of a Compton cloud around the compact object (ST80). Our analyses showed that there are up to two seed photon components in nmCVs presumably coming from the internal and outer parts of the TL. The corresponding components are the results of the Comptonization of these soft photons, characterized by their color temperature kT_{s1} and kT_{s2}, in the TL located between the WD surface and the inner part of the accretion disk. The electrons in the TL are characterized by a single electron temperature, as clearly shown by our analyses of the RXTE spectra.

The source of hard X-rays in quiescence is compact, as observed by X-ray light curves of eclipsing DNe (see, e.g., Lewin & van der Klis 2006; Mukai 2017, and references therein). Therefore, the Comptonized cloud (TL) should be compact. In our interpretation, the seed photon component showing the lowest temperatures ($kT_{s1} \sim 0.1$–0.2 keV) is coming from the inner part of the accretion disk, while the second and transient component related to kT_{s2} is coming from a more internal part of the system, closer to or from the WD surface.

For the XMM-Newton and RXTE spectra, we tested whether an addition of an interstellar absorption component (TBABS model in XSPEC) would result in lower temperatures. We freeze the interstellar absorption parameter (NH) to the value expected in the line of sight of the source. In the XMM-Newton spectra, we easily obtained satisfactory fits for the VW Hyi, U Gem, and SS Aur sources. In these cases, kT_{s1} assumed values of ~0.01 keV, but in addition to the observed increase of χ^2_{red}, this parameter was not well constrained by the fit. In the RXTE spectra, the inclusion of the TBABS component did not change the best-fit parameters. We obtained the same result when setting NH as a free parameter: in some of the fits, it assumed a very low value of 10^{19} atoms cm^{-2} and did not affect the best-fit parameters in all fits.

Figure 8 shows the total 0.4–150 keV spectrum of SS Cyg in quiescence. This spectrum corresponds to the simultaneous observations of Chandra HETG/ACIS ObsID 646 and RXTE (PCA and HEXTE) ObsID 50012-01-01-00. It is important to point out that the spectral analysis considering the simultaneous hard X-ray spectral band (>15 keV) of RXTE is superior and of great importance to constraining the physical parameters, e.g., the temperature of the electrons in the TL ($kT_e = 33^{+3}_{-3}$ keV) and the spectral index ($\Gamma = 1.8^{+0.1}_{-0.1}$), since considering only the HETG/ACIS spectrum leads to lower values of kT_e and Γ ($kT_e = 5$ keV and $\Gamma = 1.55^{+0.02}_{-0.03}$), whereas the soft spectral band of Chandra allows a better determination of the seed photon temperature kT_{s1} (see Tables 5 and 7).

The possible change in the spectral description in CVs (from optically thin thermal plasma to upscattering of soft photons due to inverse Compton in a thick Comptonization cloud) is analogous to adopting the Comptonization model to describe LMXB spectra in the ~3–50 keV energy range; before Comptonization was broadly accepted, bremsstrahlung was the model used to describe the spectra of LMXBs (see, e.g., D'Amico et al. 2001). In a similar way, bremsstrahlung is the radiative process on the basis of the MEKAL and cooling flow models that has been used to fit the spectral continuum of CVs. In LMXBs, the use of the Comptonization model was extended to broader (from ~0.3 to ~250 keV) X-ray energy bands (see,

Table 9
Best-fitting Plasma Temperature kT in the nmCVs of Our Sample Obtained by Thermal Comptonization (This Paper) and Some Previous Modeling (See Section 2)

Source	State	kT[a] (keV)	Spectral Model	Observatory	Reference
U Gem	q[c]	20	MKCFLOW	Chandra/HETG	Mukai et al. (2003; ObsID 647)
	q	55^{+10}_{-10}	MKCFLOW	XMM-Newton/EPIC	Pandel et al. (2005)
	q	15–38	CEMEKL, MKCFLOW	XMM-Newton/EPIC Chandra/HETG	Güver et al. (2006; ObsIDs 0110070401, 647)
	o[d]	5.4–29	CEMEKL	Chandra/HETG	Güver et al. (2006; ObsID 3767)
	q	$25.82^{+1.98}_{-1.43}$	MKCFLOW	XMM-Newton/EPIC	Byckling et al. (2010)
	q	$0.78^{+0.03}_{-0.01}$	MEKAL	XMM-Newton/EPIC	Byckling et al. (2010)
	q	$16.5^{+4.49}_{-3.31}$	APEC	Suzaku/XIS	Xu et al. (2016)
	q	$6.43^{+0.06}_{-0.06}$	COMPTT	XMM-Newton/EPIC	This paper (ObsID 0110070401)
	q	$5.0^{+0.5}_{-0.5}$	COMPTT	Chandra/HETG	This paper (ObsID 647)
	o	6^{+5}_{-2}	COMPTT	Chandra/HETG	This paper (ObsID 3767)
	o	43^{+5}_{-4}	COMPTT	RXTE/PCA	This paper (ObsID 80011-01-02-00)
SS Cyg	q	80	MKCFLOW	Chandra/HETG	Mukai et al. (2003; ObsID 646)
	q	$20.4^{+4.0(\mathrm{stat})+3.0(\mathrm{sys})}_{-2.6(\mathrm{stat})+3.0(\mathrm{sys})}$	CVMEKAL	Suzaku/XIS	Ishida et al. (2009)
	o	$6.0^{+1.3}_{-0.2}$	CVMEKAL	Suzaku/XIS	Ishida et al. (2009)
	q	$10.44^{+0.16}_{-0.17}$	MEKAL	Suzaku/XIS	Byckling et al. (2010)
	q	$41.99^{+1.20}_{-0.76}$	MKCFLOW	Suzaku/XIS	Byckling et al. (2010)
	o	$8.15^{+1.23}_{-0.91}$	APEC	Suzaku/XIS	Xu et al. (2016)
	q	$7.64^{+0.05}_{-0.05}$	COMPTT	XMM-Newton/EPIC	This paper (ObsID 0111310201)
	q	5[b]	COMPTT	Chandra/HETG	This paper (ObsID 646)
	o	5[b]	COMPTT	Chandra/HETG	This paper (ObsID 648)
	o	5[b]	COMPTT	Chandra/HETG	This paper (ObsID 2307)
	o	25^{+1}_{-1}	COMPTT	RXTE/PCA	This paper (ObsID 10040-01-01-000)
	o	$5.3^{+0.3}_{-0.3}$	COMPTT	RXTE/PCA	This paper (ObsID 10040-01-01-001)
	o	$5.4^{+0.3}_{-0.3}$	COMPTT	RXTE/PCA	This paper (ObsID 10040-01-01-00)
	q	$32.8^{+0.5}_{-0.6}$	COMPTT	Chandra/RXTE[e]	This paper[e]
VW Hyi	q	>5	Bremsstrahlung	EXOSAT	van der Woerd & Heise (1987)
	q	$2.17^{+0.15}_{-0.15}$	Raymond–Smith	ROSAT	Belloni et al. (1991)
	?	4–10	Two-MEKAL or Raymond–Smith	ASCA	Hasenkopf & Eracleous (2002)
	q	6–8	CEMEKL, CEVMKL, and MKCFLOW	XMM-Newton/EPIC	Pandel et al. (2003; ObsID 0111970301)
	q	$8.2^{+0.3}_{-0.3}$	MKCFLOW	XMM-Newton/EPIC	Pandel et al. (2005; ObsID 0111970301)
	q	$5.79^{+4.71}_{-2.14}$	APEC	Suzaku/XIS	Xu et al. (2016)
	q	$8.58^{+0.14}_{-0.14}$	COMPTT	XMM-Newton/EPIC	This paper (ObsID 0111970301)
	q	5–9	CEVMKL, VMCFLOW	XMM-Newton/EPIC Suzaku/XIS	Nakaniwa et al. (2019; ObsID ID 0111970301)
SS Aur	q	$6.35^{+0.40}_{-0.40}$	MEKAL	Suzaku/XIS	Byckling et al. (2010)
	q	$23.47^{+4.01}_{-3.02}$	MKCFLOW	Suzaku/XIS	Byckling et al. (2010)
	q	$8.48^{+5.34}_{-2.61}$	APEC	Suzaku/XIS	Xu et al. (2016)
	q	$6.12^{+0.13}_{-0.13}$	COMPTT	XMM-Newton/EPIC	This paper (ObsID 0502640201)
	q	37^{+6}_{-5}	COMPTT	RXTE/PCA	This paper (ObsID 30026-03-01-00)

Notes.
[a] For multitemperature plasma models, the temperature kT corresponds to the maximum temperature ($kT_{\max}$) to which the plasma is heated up.
[b] Parameter frozen.
[c] Source observed in quiescent state.
[d] Source observed in outburst state.
[e] Simultaneous Chandra HETG/ACIS ObsID 646 and RXTE (PCA and HEXTE) ObsID 50012-01-01-00.

e.g., Di Salvo et al. 2006; D'Aí et al. 2007; Montanari et al. 2009; Maiolino et al. 2013; Titarchuk et al. 2014).

As we demonstrated in Figure 9, the observed photon index Γ is distributed around 1.8 using the data for at least 15 spectra of nmCVs. Moreover, in Section 5 we theoretically estimated the photon index of the emergent spectrum, Γ, which is formed in the TL around a WD. In order to do this, we apply the radiative transfer formalism to solve the boundary problem for the energy density distribution in the TL around a WD (see Equations (2)–(5)) and estimate the gravitational energy release Q in the TL in order to find a Comptonization parameter presented by Equation (8). Moreover, solving the eigenvalue problem for an average intensity $J(\tau)$ (see Equation (10)) and using a formula for the spectral index α ($\Gamma = \alpha + 1$), Equation (13) along with Equation (8), we obtain that the photon index Γ in the TL of an accreting WD should be around 1.85. This is a first-principle estimate of the photon index, which is really confirmed by our analysis of the nmCV observations (see Figure 9).

6.1. Emission Lines and Continuum

The total observed spectrum consists of the continuum and line photon emission. In the standard framework, since the total spectrum shows many lines coming from different elements and ionization degrees, optically thin plasma with different temperatures (besides the one driving the continuum emission) is needed to describe all of the spectral features. The different plasma temperature regions are located outside of the TL where the continuum is produced. As previously mentioned, spectral fittings using a single optically thin plasma are also used to describe the total spectrum. Though it can lead to a satisfactory fit, in terms of χ^2 statistics, it can also lead to plasma temperatures too high to explain the presence of all emission lines. For example, for U Gem, a best-fit plasma temperature of about 16.5 keV (see Section 2.1 and Xu et al. 2016) is reported; at this temperature, the plasma would be completely ionized, and no line(s) in the ∼6.4–6.7 keV range would be present. That is, at this temperature, the ∼6.4–6.7 keV iron emission complex should not be produced in the same region of the X-ray continuum. Namely, much higher plasma temperatures are reported in IPs (Xu et al. 2016).

In the framework of the continuum production through the thermal Comptonization, the continuum is formed in the TL, in an optically thick medium, in both the quiescent and outburst states. The emission lines are likely produced in an optically thin region located in an external region far from the TL and the WD surface. In other words, the continuum is formed closer to the WD than the lines.

Optically thin thermal plasma and cooling flow codes make simultaneous fits of the continuum and emission lines from several elements using a range of temperatures (or a few components of optically thin thermal plasma of different temperatures). They satisfactory fit all (or almost all) excesses (features) superposing the continuum. For example, the MEKAL model includes ∼2409 lines from the 15 most important chemical elements (H, He, C, N, O, Ne, Na, Mg, Al, Si, S, Ar, Ca, Fe, and Ni), and broad residual excesses might be fitted by several narrower emission lines. Changing a description of the continuum to the Comptonization one has the consequence that the residual excesses present in the spectra (i.e., the emission lines and their shape) will be directly observed after fitting the continuum, as is observed in LMXBs. In this case, each of the emission lines should be independently identified and modeled using, e.g., Gaussian components.

Applying a thermal Comptonization component (either COMPTT or COMPTB) to fit the continuum of the nmCVs, we have identified a broad and strong emission line peaked at ∼0.96–1.02 keV in all XMM-Newton spectra. We fitted this residual excess presented in the ∼0.8–1.2 keV energy range using a single Gaussian line. We also identified the centroid energy of the lines as being compatible with resonance lines emitted by Fe XXI (in SS Aur, U Gem, and VW Hyi), Fe XVII (in VW Hyi, SS Aur, and SS Cyg), and/or Ne X (in VW Hyi and U Gem; see Table 3). This residual excess was also observed in one Chandra HETG/ACIS spectrum of U Gem (ObsID 3767) and two SS Cyg spectra in outburst. In these cases, the excess appears peaked at $\sim 1.01 \pm 0.01$ keV. In U Gem, the centroid energy of the Gaussian component fitted to this excess is compatible with the Ne X, Fe XVII, and Fe XXI lines. In SS Cyg, this excess is compatible with emission lines from: either Ca XVIII, Fe XVII, Ni XIX, or Ni XVIII in ObsID 648; and either Ca XVIII, Ni XIX, or Ne IX in ObsID 2307. Other lines, compatible with emission from Mg XI, Mg XII, Si XIII, and Fe XXII, were also observed in the Chandra spectra; see Table 6. The observation of this broad feature around 1.01 keV in both XMM-Newton EPIC-pn and HETG/ACIS spectra and its variability indicate that this feature is not a systematic effect of our spectral modeling or an individual issue of one of the instruments.

It is important to point out that this broad excess likely corresponds to a blend of narrow lines emitted by Fe XVII, XIX, XX, and XXI; Ne IX–X; and/or Ni XIX ions, which are not very well resolved by the medium energy resolution of the pn camera and HETG/ACIS. Several lines are observed in this soft X-ray energy range by the LETG/HRC grating spectrometer (due its resolving power >1000; see also, e.g., Mukai et al. 2003; Pandel et al. 2003). For example, in our analysis of the LETG/HRC SS Cyg spectrum, lines at ∼0.82, ∼0.92, and ∼1.0 keV were clearly present.

7. Summary and Conclusions

The thermal Comptonization model plus Gaussian components (used to account for the emission lines) can successfully describe the spectra of the nmCVs in our source sample. Though we did not find a perfect fit, in terms of χ^2 statistics, to the XMM-Newton spectra of VW Hyi and U Gem, both the Chandra HETG/ACIS and RXTE PCA spectra of the latter source were satisfactory fitted by our Comptonization model. It is likely that the presence of many lines, besides the iron complex, in the XMM-Newton spectra of VW Hyi and U Gem worsened the fit quality.

The XMM-Newton and Chandra spectra show a similar range of physical parameters. However, due to the broader spectral energy range, the RXTE spectra provided a better description of the Comptonization effect and determination of the physical parameters. We found that two Comptonization components are necessary to successfully fit the simultaneous 0.4–150 keV Chandra/RXTE spectra of SS Cyg in quiescence and two 2.5–25 keV RXTE spectra of SS Cyg in outburst. In this case, the best fits are found only if the optical depth and plasma temperature of the Compton cloud are the same for these two components. As a result, we found that only one photon index, $\Gamma \sim 1.8$, is capable of describing the total spectra of all analyzed nmCVs.

Two blackbody components of seed photons are characterized by their color temperature (kT_{s1} and kT_{s2}). In our interpretation, the seed photon component showing the lowest temperatures ($kT_{s1} \sim 0.1$–0.2 keV) is presumably coming from the inner part of the accretion disk or outer part of the TL, while the second and transient component related to kT_{s2} is coming from a more internal part of the system, closer to the WD surface. We think that these temperatures are related to the innermost part of the corona (TL), rather than associated with a WD surface; otherwise, a value of $kT_{s2} \sim 0.6$–0.8 keV could exceed the appropriate temperature limit for the existence of bounded atmospheres on WDs.

The seed photons are upscattered by hot electrons in the TL characterized by a single electron temperature kT_e (in the 5–48 keV range) and located between the disk and the WD surface. The TL optical depth changes in the wide range $1 \lesssim \tau_0 \lesssim 5$.

When we compared the physical parameters between different sources in different states, we did not find any correlation of Γ (or $\alpha = \Gamma - 1$) with the plasma temperature

kT_e (see Figure 9) or a clear correlation of physical parameters with source stage. However, the RXTE observations of SS Cyg show a clear change of the electron temperature in the Compton cloud (or TL) when the source is found in different states: it is higher in quiescence, 33^{+3}_{-3} keV; decreases to 25^{+1}_{-1} keV at the initial stage of the optical outburst; and reaches $\sim 5.5^{+0.4}_{-0.3}$ keV during a rise of the outburst. This decrease in the electron temperature can explain the suppression of hard X-rays ($\gtrsim$25 keV) during outburst in SS Cyg. Therefore, the dependence of the physical parameters on the source stages may depend on the source.

Finally, we conclude that our two thermal Comptonization component model using a single thermal plasma temperature and optical depth plus Gaussian components can describe the 0.4–150 keV spectra of nmCVs in both the quiescent and outburst states without evoking more than one optically thin plasma temperature or cooling flow model.

Moreover, we develop the radiative transfer model that rigorously demonstrates and explains our main observational result using the first-principle arguments that the photon indices Γ in WDs should be around 1.8 (see Figure 9).

T.M. acknowledges the financial support given by the Erasmus Mundus Joint Doctorate Program by grant No. 2013-1471 from the EACEA of the European Commission and the INAF/OAS Bologna. T.M. acknowledges the support given by the National Program on Key Research and Development Project (grant No. 2016YFA0400803) and the NSFC (11622326 and U1838103). T.M. also thanks the High Energy Astrophysics group of the Physics Dept. of Ferrara University, INAF/OAS Bologna, and Wuhan University for the warm hospitality and support. L.T. appreciates the interest and support of his colleagues from the Physical Institute of the Russian Academy of Science (FIAN). M.O. acknowledges support from the Italian Space Agency under grant ASI-INAF 2017-14-H.0. The authors are grateful to the anonymous referee for the constructive suggestions.

ORCID iDs

T. Maiolino https://orcid.org/0000-0002-4918-7182
L. Titarchuk https://orcid.org/0000-0002-9998-7591
F. D'Amico https://orcid.org/0000-0003-1304-9914
Z. Q. Cheng https://orcid.org/0000-0002-9983-8609
W. Wang https://orcid.org/0000-0003-3901-8403
M. Orlandini https://orcid.org/0000-0003-0946-3151
Filippo Frontera https://orcid.org/0000-0003-2284-571X

References

Barlow, R. 1989, Statistics. A Guide to the Use of Statistical Methods in the Physical Sciences (New York: Wiley)
Baskill, D. S., Wheatley, P. J., & Osborne, J. P. 2005, MNRAS, 357, 626
Belloni, T., Verbunt, F., Beuermann, K., et al. 1991, A&A, 246, L44
Byckling, K., Mukai, K., Thorstensen, J. R., & Osborne, J. P. 2010, MNRAS, 408, 2298
D'Aí, A., Życki, P., Di Salvo, T., et al. 2007, ApJ, 667, 411
D'Amico, F., Heindl, W. A., Rothschild, R. E., & Gruber, D. E. 2001, ApJL, 547, L147
Di Salvo, T., Goldoni, P., Stella, L., et al. 2006, ApJL, 649, L91
Done, C., & Osborne, J. P. 1997, MNRAS, 288, 649
Farinelli, R., & Titarchuk, L. 2011, A&A, 525, A102
Farinelli, R., Titarchuk, L., Paizis, A., & Frontera, F. 2008, ApJ, 680, 602
Friend, M. T., Martin, J. S., Connon-Smith, R., & Jones, D. H. P. 1990, MNRAS, 246, 654
George, I. M., & Fabian, A. C. 1991, MNRAS, 249, 352
Godon, P., & Sion, E. M. 2005, MNRAS, 361, 809
Guainazzi, M. 2016, XMM-Newton Calibration Technical Note, XMM-SOC-CAL-TN-0018, ESA-ESAC, https://xmmweb.esac.esa.int/docs/documents/CAL-TN-0018.pdf
Güver, T., Uluyazı, C., Özkan, M. T., & Göğüş, E. 2006, MNRAS, 372, 450
Harrison, T. E., Johnson, J. J., McArthur, B. E., et al. 2004, AJ, 127, 460
Harrison, T. E., McNamara, B. J., Szkody, P., et al. 1999, ApJL, 515, L93
Harrison, T. E., McNamara, B. J., Szkody, P., & Gilliland, R. L. 2000, AJ, 120, 2649
Hasenkopf, C. A., & Eracleous, M. 2002, BAAS, 34, 1301
Hua, X.-M., & Titarchuk, L. 1995, ApJ, 449, 188
Ishida, M., Okada, S., Hayashi, T., et al. 2009, PASJ, 61, S77
Iyer, N., Mukherjee, D., Dewangan, G. C., Bhattacharya, D., & Seetha, S. 2015, MNRAS, 454, 741
Lewin, W. H. G., & van der Klis, M. 2006, Compact Stellar X-Ray Sources (Cambridge: Cambridge Univ. Press), 39
Liedahl, D. A., Osterheld, A. L., & Goldstein, W. H. 1995, ApJL, 438, L115
Long, K. S., Mauche, C. W., Raymond, J. C., Szkody, P., & Mattei, J. A. 1996, ApJ, 469, 841
Maiolino, T., D'Amico, F., & Braga, J. 2013, A&A, 551, L2
Maiolino, T., Laurent, P., Titarchuk, L., Orlandini, M., & Frontera, F. 2019, A&A, 625, A8
Mason, K. O., Cordova, F. A., Watson, M. G., & King, A. R. 1988, MNRAS, 232, 779
Mauche, C. W., & Raymond, J. C. 2000, ApJ, 541, 924
Mauche, C. W., & Robinson, E. L. 2001, ApJ, 562, 508
Mewe, R., Lemen, J. R., & van den Oord, G. H. J. 1986, A&AS, 65, 511
Montanari, E., Titarchuk, L., & Frontera, F. 2009, ApJ, 692, 1597
Mukai, K. 2017, PASP, 129, 062001
Mukai, K., Kinkhabwala, A., Peterson, J. R., Kahn, S. M., & Paerels, F. 2003, ApJL, 586, L77
Nakaniwa, N., Hayashi, T., Takeo, M., & Ishida, M. 2019, MNRAS, 488, 5104
Okada, S., Nakamura, R., & Ishida, M. 2008, ApJ, 680, 695
Orlandini, M., Frontera, F., Masetti, N., Sguera, V., & Sidoli, L. 2012, ApJ, 748, 86
Pandel, D., Córdova, F. A., & Howell, S. B. 2003, MNRAS, 346, 1231
Pandel, D., Córdova, F. A., Mason, K. O., & Priedhorsky, W. C. 2005, ApJ, 626, 396
Patterson, J., & Raymond, J. C. 1985a, ApJ, 292, 550
Patterson, J., & Raymond, J. C. 1985b, ApJ, 292, 535
Polidan, R. S., Mauche, C. W., & Wade, R. A. 1990, ApJ, 356, 211
Press, W. H., Teukolsky, S. A., Vettering, W. T., & Flannery, B. P. 1992, Numerical Recipes in C. The Art of Scientific Computing (2nd ed.; Cambridge: Cambridge Univ. Press)
Pringle, J. E., & Savonije, G. J. 1979, MNRAS, 187, 777
Rana, V. R., Singh, K. P., Schlegel, E. M., & Barrett, P. E. 2006, ApJ, 642, 1042
Raymond, J. C., & Smith, B. W. 1977, ApJS, 35, 419
Ritter, H., & Kolb, U. 2003, yCat, V/113A
Rothschild, R. E., Blanco, P. R., Gruber, D. E., et al. 1998, ApJ, 496, 538
Rybicki, G. B., & Lightman, A. P. 1979, Radiative Processes in Astrophysics (New York: Wiley), 393
Schoembs, R., & Vogt, N. 1981, A&A, 97, 185
Shafter, A. W., & Harkness, R. P. 1986, AJ, 92, 658
Sion, E. M., Cheng, F. H., Sparks, W. M., et al. 1997, ApJL, 480, L17
Sunyaev, R. A., & Titarchuk, L. G. 1980, A&A, 86, 121
Sunyaev, R. A., & Titarchuk, L. G. 1985, A&A, 143, 374
Szkody, P., Long, K. S., Sion, E. M., & Raymond, J. C. 1996, ApJ, 469, 834
Szkody, P., Nishikida, K., Raymond, J. C., et al. 2002, ApJ, 574, 942
Titarchuk, L. 1994, ApJ, 434, 570
Titarchuk, L., & Lyubarskij, Y. 1995, ApJ, 450, 876
Titarchuk, L., Seifina, E., & Shrader, C. 2014, ApJ, 789, 98
van der Woerd, H., & Heise, J. 1987, MNRAS, 225, 141
Warner, B. 1987, MNRAS, 227, 23
Warner, B. 1995, Cataclysmic Variable Stars (Cambridge: Cambridge Univ. Press)
Williams, G. A., King, A. R., & Brooker, J. R. E. 1987, MNRAS, 226, 725
Xu, X.-j., Wang, Q. D., & Li, X.-D. 2016, ApJ, 818, 136